

# A reactive force field molecular dynamics study on the inception mechanism of titanium tetraisopropoxide (TTIP) conversion to titanium clusters

Dingyu Hou<sup>a</sup>, Muye Feng<sup>b</sup>, Jili Wei<sup>c</sup>, Yi Wang<sup>b</sup>, Adri C. T. van Duin<sup>d</sup>, Kai H. Luo<sup>a,\*</sup>

<sup>a</sup>*Department of Mechanical Engineering, University College London, Torrington Place, London WC1E 7JE, United Kingdom*

<sup>b</sup>*Center for Combustion Energy, Key Laboratory of Thermal Science and Power Engineering of Ministry of Education, Department of Energy and Power Engineering, Tsinghua University, Beijing 100084, China*

<sup>c</sup>*Department of Engineering, University of Cambridge, Trumpington Street, Cambridge CB2 1PZ, United Kingdom*

<sup>d</sup>*Department of Mechanical Engineering, The Pennsylvania State University, State College, Pennsylvania 16802, United States*

---

## Abstract

We performed ReaxFF reactive molecular dynamics simulations to investigate the inception mechanism of TTIP precursor droplet conversion to Ti-containing clusters in 1000 K–2500 K with or without gaseous O<sub>2</sub> molecules. A new Ti/C/H/O ReaxFF force field has been developed. Key intermediate titanium species and the initial decomposition pathways of TTIP are identified. The effects of temperature, O<sub>2</sub> concentration and high-temperature residence time on the conversion of TTIP to incipient titanium clusters are investigated. Results suggest that high pyrolysis temperature does not necessarily promote the formation of incipient Ti-containing clusters, due to less stable Ti-O bonds at high temperatures. Ti<sub>2</sub>O<sub>x</sub>C<sub>y</sub>H<sub>z</sub> species appear earlier than TiO<sub>2</sub> during TTIP pyrolysis, while TiO<sub>2</sub> forms earlier than Ti<sub>2</sub>O<sub>x</sub>C<sub>y</sub>H<sub>z</sub> species and has much higher concentration with ambient O<sub>2</sub>. Decreasing high-temperature residence time boosts the formation of Ti-containing clusters by facilitating the condensation of TiO<sub>2</sub> vapors. The growth pattern of the incipient titanium clusters is elucidated as formation of

---

\*Corresponding author

*Email address:* [k.luo@ucl.ac.uk](mailto:k.luo@ucl.ac.uk) (Kai H. Luo)

Ti-O bond with  $\text{TiO}_x\text{C}_y\text{H}_z$  species or titanium clusters followed by continuous breakage of Ti-O or C-O bonds to release hydrocarbon moieties.

*Keywords:* ReaxFF, Reactive molecular dynamics simulation, TTIP, titanium dioxide nanoparticles, inception mechanism

---

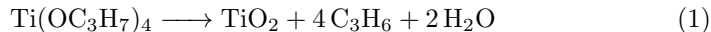
## 1. Introduction

Titanium dioxide nanoparticles ( $\text{TiO}_2$  NPs) are one of the most functionally versatile metal oxide nanomaterials [1–3]. In addition to its traditional usage for pigments, semi-conductors and catalysis,  $\text{TiO}_2$  NPs also find novel applications in emerging areas such as photocatalysis [4, 5], gas-sensors [6, 7], waste water treatment [8, 9], biomaterial coatings [10–12].  $\text{TiO}_2$  NPs are routinely manufactured through flame reactors in industry by combusting titanium tetrachloride ( $\text{TiCl}_4$ ) vapors [13, 14]. Compared with the wet chemistry route, the one-step flame synthesis can produce nanopowders of high purity at high throughput, along with uniquely desired particle structures and without liquid by-products [3, 15]. Besides vapor-fed flame synthesis [16],  $\text{TiO}_2$  NPs can also be synthesized by combustion of sprays, i.e., the so-called flame spray pyrolysis (FSP) [13, 17]. FSP is becoming more attractive recently due to its broader spectrum of liquid precursors than conventional vapor flame reactors, which makes it suitable to synthesize multicomponent ceramics and metals with specifically designed structures [3, 17–19]. Besides  $\text{TiCl}_4$ , titanium tetraisopropoxide ( $\text{Ti}(\text{OC}_3\text{H}_7)_4$ , TTIP) also appears to be a promising precursor as it is safer and environmentally more friendly [19–27].

Since the properties of product nanoparticles dictate their end-use, actively controlling the characteristics of the synthesized  $\text{TiO}_2$  nanomaterials is desired in order to meet a variety of applications both in industry and daily life. Hence, understanding the formation mechanism of flame synthesized NPs is of vital importance, otherwise properties of the product nanomaterials will have to be manipulated based on trial and error. In order to explore the formation mechanism of FSP synthesized  $\text{TiO}_2$  NPs, much experimental work has been done

focusing on the influence of various tunable factors [13] (such as flame temperature [28, 29], pressure [30], high-temperature residence time [21], dispersion gas flow rate [20, 29], oxygen and precursor concentration [28, 29], etc.) on the properties (i.e., size, shape and crystalline composition) of the product TiO<sub>2</sub> NPs. These experimental studies in combination with continuous modelling efforts [13, 17, 31–35] have provided a scientific basis of FSP synthesized nanoparticles [3]. For example, currently it is well recognized that the competition between sintering and coagulation determines the morphology of flame synthesized NPs, and significance of these two processes can be affected by flame temperature and particle residence time [17, 36]. Such knowledge is beneficial for rational design and operation in manufacturing TiO<sub>2</sub> NPs industrially.

However, open questions still remain regarding the inception process of FSP synthesized TiO<sub>2</sub> NPs, mainly due to the difficulty to measure or capture the extremely fast droplet-to-particle conversion process in high-temperature flame experimentally. Because of the lack of knowledge on detailed inception mechanism from TTIP precursor to TiO<sub>2</sub> NPs in flames, most existing modelling studies [31, 32, 37, 38] simply use a one-step global reaction



to describe the decomposition of TTIP, which was first proposed by Okuyama et al. [39]. Okuyama et al. [39] also calculated the overall rate constants of Reaction (1) by measuring the concentration of propylene (C<sub>3</sub>H<sub>6</sub>) versus time, which was widely used in population balance models for flame synthesized TiO<sub>2</sub> NPs [31, 32, 37, 38]. However, Okuyama et al. [39] conducted experiment in a laminar flow reactor where temperature was around 800 K. This value can be much lower than the temperature in typical flame reactors, where the peak temperature can be higher than 2500 K. As such, it is uncertain whether the rate constant reported by Okuyama et al. [39] can be extrapolated to model synthesis of TiO<sub>2</sub> NPs using TTIP as a precursor through the FSP technology.

Efforts towards building a detailed decomposition mechanism of TTIP have been made by Buerger et al. [23], who systematically calculated the thermo-

chemical data of 981 Ti-containing candidate species on the basis of the thermal breakage of bonds within a TTIP molecule at density functional theory (DFT) level. They then proposed a thermodynamically consistent mechanism with  $\text{Ti}(\text{OH})_4$  being the final product before conversion to  $\text{TiO}_2$  to describe the thermal decomposition of TTIP [24]. However, the mechanism over predicted the ignition delay for TTIP by an order of magnitude and the authors attributed the discrepancy to the possible loss of chemical pathways.

Ershov et al. [40] conducted UV-photodissociation experiment on TTIP molecules under molecular-beam conditions. Using the time-of-flight mass spectrometer (TOF-MS) technique, Ti and TiO were detected among the most abundant photofragments, while  $\text{TiO}_2$  was hardly found. With the aid of quantum chemistry calculation, Ershov et al. [40] proposed a new decomposition pathway of TTIP through acetone-elimination reaction, which was contrary to the existing data in the literature. Ti and TiO were also detected during combustion of TTIP in a premixed flat burner-stabilized  $\text{H}_2/\text{O}_2/\text{Ar}$  flame using the flame-sampling molecular beam mass-spectrometry [41]. Besides Ti and TiO, Shmakov et al. [41] also reported the mass peak intensity profiles of some other titanium-containing species including  $\text{TiO}_2$ ,  $\text{Ti}(\text{OH})\text{O}$ ,  $\text{Ti}(\text{OH})$ ,  $\text{TiH}$ ,  $\text{Ti}_2\text{O}_3$  and  $\text{TiO}_3$ .

In addition to the above mentioned gaseous Ti-containing species, recently Fang et al. [42] measured charged clusters in a premixed  $\text{CH}_4/\text{O}_2/\text{N}_2$  flame with TTIP addition using an atmospheric pressure interface time-of-flight (Api-TOF) mass spectrometer. Surprisingly, pure  $\text{TiO}_2$  clusters were not detected. In addition, their experimental results showed that intermediates from TTIP decomposition may polymerize or aggregate into larger clusters prior to conversion to pure  $\text{TiO}_2$ .

To briefly summarize, despite great progress made in studying the phenomena of FSP synthesized  $\text{TiO}_2$  NPs over the past several decades, the decomposition mechanism of TTIP has not been fully understood yet, especially regarding the inception mechanism of TTIP conversion to  $\text{TiO}_2$  NPS in high-temperature flames. Moreover, experimental studies have already demonstrated that a se-

ries of operation factors such as flame temperature, particle high-temperature residence time, oxygen concentration and etc., can affect the size, shape and crystal phase of FSP synthesized  $\text{TiO}_2$  NPs [20, 28, 43, 44]. Hence a further question can be asked — Do these factors affect the inception mechanism of TTIP conversion to  $\text{TiO}_2$  NPs? Or do they only affect the processes at a later stage, i.e., coagulation and sintering?

Being intrigued by the above mentioned unresolved issues, in this study, we will focus on examining the initial stages of TTIP precursors conversion to incipient titanium clusters in the context of FSP using ReaxFF reactive molecular dynamics simulation [45]. MD simulations provide an ideal approach for investigating processes happening at nanoscales. For examples, previous studies have examined coagulation [46], sintering/coalescence [47–49], crystal phase transformation [48, 49] and surface coating by aerosol deposition [12] of  $\text{TiO}_2$  NPs using classical MD simulations, and valuable insights have been obtained. However, chemical reactions are generally excluded in classical MD simulations, although in a recent study, Jami and Jabbarzadeh [12] have identified formation of Ti-O and Ti-Ti bonds by introducing predefined cutoff lengths while simulating  $\text{TiO}_2$  NPs depositing on a titanium substrate using a sophisticated MEAM potential. With the aid of ReaxFF reactive MD simulation [45, 50], which allows bond breaking and forming, we are able to explore the initial stages of nanoparticle formation in high-temperature flame at the atomic level. Most recently, Wei et al. [51] have investigated the hydrolysis of TTIP using ReaxFF MD simulations. The second-order hydrolysis rate constant was estimated and the formation pathway of early Ti-containing clusters were illustrated, manifesting the capability of reactive MD simulations on exploring the detailed mechanism of precursor molecules converting to early metal oxide clusters in high-temperature flame.

In this work, we start from simulating the pyrolysis of a TTIP precursor nanodroplet at different temperatures ranging from 1500 K to 2500 K, which practically cover typical temperatures during synthesis of  $\text{TiO}_2$  NPs through FSP [13]. Then different concentrations of  $\text{O}_2$  are added into the simulation

system to study the effect of O<sub>2</sub> concentration on the inception mechanism of TTIP to TiO<sub>2</sub> NPs. In addition, predefined temperature profiles in the range of 1000 K to 2500 K with different high-temperature residence time are imposed to investigate its influence of on the inception process of TTIP.

## 2. Simulation Methods

### 2.1. Ti/C/H/O ReaxFF force field

ReaxFF reactive MD simulations in this work are performed using the Large-scale Atomic/Molecular Massively Parallel Simulator (LAMMPS) package [52] implemented with reax/c [53, 54]. ReaxFF is a general bond-order-dependent force field that enables the descriptions of bond breaking and bond formation. Details about the formulation of the ReaxFF reactive force field method can be found in Refs. [45, 53]. In current work, The parameters of the Ti/C/H/O ReaxFF force field are re-optimized on the basis of two existing ReaxFF force fields, the CHON-weak force field [55] and the force field for MXene materials (Ti<sub>n+1</sub>C<sub>n</sub>T<sub>x</sub>, T<sub>x</sub> = -O, -OH or -F) [56–59]. More specifically, the interactions between Ti and C/H/O atoms are based on the description of the MXene force field while the interactions between C/H/O atoms follow the description of the CHON-weak force field. The parameters of this newly developed Ti/C/H/O ReaxFF force field are provided in the Supporting Information. The MXene force field has been successfully employed to investigate various properties of different systems containing MXene materials, such as the dynamics of aqueous electrolytes confined in two-dimensional-TiO<sub>2</sub>/Ti<sub>3</sub>C<sub>2</sub>T<sub>2</sub> MXene heterostructures [56], the interaction between MXene and solvents [60], the fundamental mechanical properties of MXene [61], etc. Most recently and more relevant to the system being investigated in this work, Wei et al. [51] have used the MXene force field to study the kinetics of hydrolysis reactions of gas-phase TTIP through ReaxFF MD simulation. Instead of using the MXene force field directly, we re-optimized the parameters for C/H/O interactions in it based on the CHON-weak force field because the latter has a better performance for

describing the hydrocarbon/water weak interactions in condensed phase [55]. This merit is desired in this study as we shall start simulation from a TTIP droplet rather than gas-phase TTIP molecules in order to mimic the process that precursor droplets enter into the hot flame region during FSP.

To test the performance of this newly developed Ti/C/H/O ReaxFF force field, we have calculated the density ( $\rho$ ) and boiling point ( $T_b$ ) of bulk phase TTIP at 1 atm pressure by MD simulation and compared the results with experimental data. Both the calculated density and boiling point agree well with experimental data. (At 300 K,  $\rho = 0.96 \text{ g cm}^{-3}$  based on MD simulation while  $\rho = 0.95 \text{ g cm}^{-3}$  based on experimental measurements [22];  $T_b = 562 \text{ K}$  obtained by MD simulation while  $T_b = 505 \text{ K}$  based on experimental data [62]). More details about the calculation of density and boiling point are provided in the Supporting Information (see Fig. S1 and Fig. S2). In addition to the physical properties of condensed phase TTIP, we also estimated the first order pyrolysis rate constants of gas-phase TTIP by reactive MD simulation and compared our results with previous work. Simulation details on calculating gas-phase TTIP pyrolysis rate constants are described in Supporting Information. **As shown in Fig. S4**, the pyrolysis rate constants obtained in this work are very close to the results reported by Wei et al. [51], which were also based on MD simulation with a different temperature range (1300 K–2500 K in this work versus 1500 K–3000 K used by Wei et al. [51]) and a different Ti/C/H/O force field (i.e., the aforementioned MXene force field [57–59]). The difference between the activation energy for TTIP pyrolysis (which can be calculated based on the slope of the  $\ln k - 1/T$  plot), reported by Wei et al. [51] and that obtained in this work  $< 4 \text{ kcal/mol}$ , which is within the range of uncertainty of energy for ReaxFF MD simulations. The slightly difference in the activation energy can be attributed to the different parameters describing C/H/O interaction and the different temperature range used in calculating rate constants  $k$ . Rate constants of TTIP pyrolysis estimated based on experiments conducted in a laminar flow reactor with a relatively low temperature range (500 K–670 K) [39] are also plotted in Fig. S4. As suggested by Fig. S4, extrapolating the experimental data of

Okuyama et al. [39] to high temperature region leads to rate constant  $k$  much lower than that obtained based on MD simulations, which again highlights the need to investigate the detailed decomposition mechanism and the inception mechanism of TTIP conversion to incipient titanium clusters in the hot flame region.

## 2.2. Simulation setup

Since this work intended to provide insights into TTIP inception mechanism in the context of FSP, in which precursor spray droplets are combusted in high-temperature flame, we started simulation from a TTIP nanodroplet instead of gas-phase TTIP molecules that were used previously when calculating the pyrolysis rate constants of TTIP in Section 2.1. Initial configuration of the TTIP nanodroplet is generated using the PACKMOL program [63] by randomly packing 130 TTIP molecules within a confined spherical region with a diameter = 6 nm, leading to a density slightly lower than the density of liquid TTIP at 300 K. After using the conjugate gradient (CG) algorithm to eliminate artifacts of the initialization, the system is further equilibrated at 300 K for 350 ps. Figure S5 in the Supporting Information shows the potential energy of the system versus simulation time during equilibration, which suggests that TTIP<sub>130</sub> droplet achieves equilibrium state at 300 K after about 100 ps, as the potential energy of the system becomes nearly unchanged with time after then. Three equilibrated configurations of TTIP<sub>130</sub> are chosen randomly (uniform distribution) as the initial configurations of the TTIP droplet in the following pyrolysis and oxidation simulations. The canonical ensemble (i.e., controlled particle number, volume and temperature, NVT) is used during the equilibration process with a 0.2 fs timestep. Constant temperature is maintained by the Nosé-Hoover thermostat with a damping constant of 20 fs.

After obtaining the equilibrated configurations of a TTIP<sub>130</sub> nanodroplet at 300 K, it is put at the center of a simulation box with side length  $L = 40$  nm. Periodic boundary conditions are used in  $x$ ,  $y$  and  $z$  directions. Eleven cases with different simulations conditions have been designed serving different pur-

poses as listed in Table 1. Cases 1, 2 and 3 are TTIP<sub>130</sub> nanodroplet pyrolysis at 1500 K, 2000 K and 2500 K respectively, the purpose of which is to study the effect temperature on the inception process of TTIP to incipient clusters. These three temperatures are chosen because 1500 K – 2500 K covers the most typical flame temperatures in FSP [13, 43]. For Cases 4, 5 and 6, different numbers of O<sub>2</sub> molecules are introduced into the simulation box, in order to study how different concentrations of O<sub>2</sub> will affect the inception process of the TTIP precursor droplet. 2340 O<sub>2</sub> molecules correspond to equivalence ratio = 1, i.e., all 130 TTIP molecules are fully oxidized to form TiO<sub>2</sub>, H<sub>2</sub>O and CO<sub>2</sub>. For Cases 7–11, different temperature profiles shown in Fig. 12(a) are imposed during the simulation, which can be used to investigate the influence of high-temperature residence time on the inception process. Figure 1 illustrates the initial config-

Table 1: Simulation setup of 11 cases with different surrounding gas and temperature profiles being investigated in this work

Case	Surrounding gas	Temperature (K)	Purpose
1		1500	
2	pyrolysis	2000	Temperature effect
3		2500	
4	2340 O <sub>2</sub>		
5	1170 O <sub>2</sub>	2500	O <sub>2</sub> concentration effect
6	585 O <sub>2</sub>		
7		$T$ profile1 <sup>1</sup>	
8		$T$ profile2 <sup>1</sup>	
9	2340 O <sub>2</sub>	$T$ profile3 <sup>1</sup>	High-temperature residence time effect
10		$T$ profile4 <sup>1</sup>	
11		$T$ profile5 <sup>1</sup>	

<sup>1</sup> Temperature profiles are shown in Fig. 12(a).

uration of the simulation system. For the three pyrolysis cases, i.e., Cases 1–3, there is no O<sub>2</sub> surrounding the TTIP<sub>130</sub> droplet; While for Cases 4–11, different

numbers of  $O_2$  are introduced in the simulation box. The simulation time for

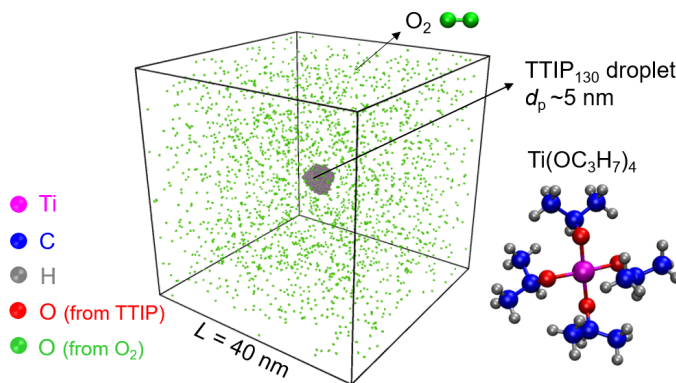


Figure 1: Illustration of the initial configuration of the simulation system. The molecular structure of an  $O_2$  molecule and a TTIP molecule are inserted.  $d_p$  is the diameter of the  $TTIP_{130}$  droplet.

each case is 6000 ps. Since the  $TTIP_{130}$  nanodroplet was equilibrated at 300 K, prior to the 6000 ps simulation, the system is rapidly heated (in 10 ps) from 300 K to the target temperatures, i.e., 1500 K, 2000 K and 2500 K. The canonical ensemble (NVT) is used to perform both pyrolysis and oxidation simulations. Temperature is controlled to the desired value by the Nosé-Hoover thermostat with a damping constant of 10 fs. A shorter simulation timestep, 0.1 fs, is used to ensure smooth evolution of reactions at the relatively high flame temperatures investigated in this work. Snapshots are prepared by Visual Molecular Dynamics (VMD) software [64] and OVITO [65]. A commonly used 0.3 bond order cutoff is employed to identify the species formed during simulation [66–71]. For post-processing of the simulation trajectories, atomic positions and bond information are collected every 1 ps and the recognized species information is collected at a higher frequency, i.e., every 0.5 ps, so as to provide more detailed insights into the reaction pathway.

### 3. Results and Discussions

#### 3.1. Pyrolysis of TTIP<sub>130</sub> – Effect of temperature

We first consider the pyrolysis of a TTIP<sub>130</sub> nanodroplet in Cases 1, 2 and 3, where O<sub>2</sub> is not introduced in the simulation system. Figure 2 shows the time evolution of normalized number of TTIP, TiO<sub>2</sub>, TiO<sub>*x*</sub>C<sub>*y*</sub>H<sub>*z*</sub>, Ti<sub>2</sub>O<sub>*x*</sub>C<sub>*y*</sub>H<sub>*z*</sub> and Ti<sub>*m*</sub>O<sub>*x*</sub>C<sub>*y*</sub>H<sub>*z*</sub> ( $m, x, y, z \in \mathbb{N}, m > 2$ ) during the pyrolysis of a TTIP<sub>130</sub> nanodroplet at three different temperatures. Note that TiO<sub>*x*</sub>C<sub>*y*</sub>H<sub>*z*</sub>, Ti<sub>2</sub>O<sub>*x*</sub>C<sub>*y*</sub>H<sub>*z*</sub> and Ti<sub>*m*</sub>O<sub>*x*</sub>C<sub>*y*</sub>H<sub>*z*</sub> do not refer to one specific species but a group of Ti-containing species that contain 1, 2 and  $m (> 2)$  Ti atoms respectively regardless of the number of O, C and H atoms. The normalized number of species  $\bar{n}$  in Fig. 2 represents the proportion of Ti element existing in the form of one specific species (i.e., TTIP or TiO<sub>2</sub>) or a certain group of species (i.e., TiO<sub>*x*</sub>C<sub>*y*</sub>H<sub>*z*</sub>, Ti<sub>2</sub>O<sub>*x*</sub>C<sub>*y*</sub>H<sub>*z*</sub> or Ti<sub>*m*</sub>O<sub>*x*</sub>C<sub>*y*</sub>H<sub>*z*</sub>). Take Ti<sub>2</sub>O<sub>*x*</sub>C<sub>*y*</sub>H<sub>*z*</sub> for an example. Assuming that at time  $t$  there are  $n$  molecules containing two Ti atoms, then the normalized number of Ti<sub>2</sub>O<sub>*x*</sub>C<sub>*y*</sub>H<sub>*z*</sub> at time  $t$  is calculated as  $2n/130$ .

It is worth noting that in Fig. 2, Ti<sub>2</sub>O<sub>*x*</sub>C<sub>*y*</sub>H<sub>*z*</sub> appears earlier than TiO<sub>2</sub>, and with its number concentration much higher than that of TiO<sub>2</sub> regardless of the pyrolysis temperature. This finding is contrary to previous understanding on the inception mechanism of TTIP conversion to TiO<sub>2</sub> nanoparticles. It was generally believed that TTIP was first converted to TiO<sub>2</sub> product vapor, then homogeneous nucleation occurred to form thermodynamically stable clusters when TiO<sub>2</sub> vapors became sufficiently supersaturated [17]. However, our simulation results suggest that TiO<sub>2</sub> monomers can only play a minor role in the inception process due to its almost negligible number concentration. Instead, the dimerization of two TiO<sub>*x*</sub>C<sub>*y*</sub>H<sub>*z*</sub> species occurs earlier and proceeds much faster than precursor TTIP molecules converting to TiO<sub>2</sub> molecules. Similar findings were also reported by Wei et al. [51] when investigating the kinetics of hydrolysis of gas-phase TTIP molecules using reactive MD simulation. Moreover, this is also consistent with the recent experimental results of Fang et al. [42], who measured the charged clusters formed in a premixed CH<sub>4</sub>/O<sub>2</sub>/N<sub>2</sub> flat

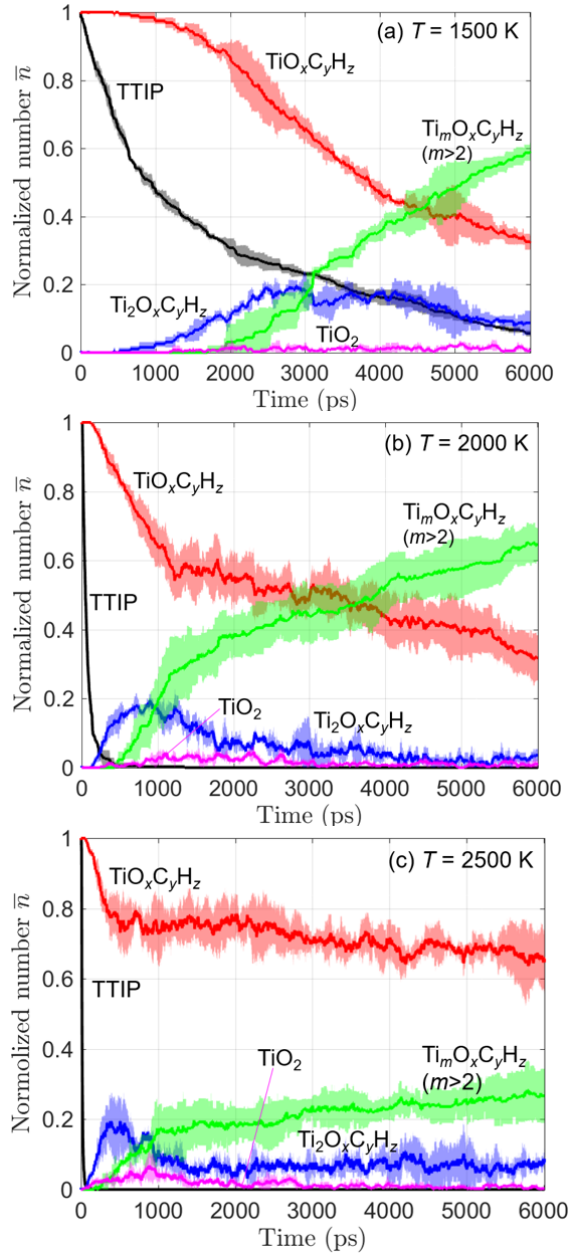


Figure 2: The normalized number  $\bar{n}$  of TTIP, TiO<sub>2</sub>, TiO<sub>x</sub>C<sub>y</sub>H<sub>z</sub>, Ti<sub>2</sub>O<sub>x</sub>C<sub>y</sub>H<sub>z</sub> and Ti<sub>m</sub>O<sub>x</sub>C<sub>y</sub>H<sub>z</sub> ( $m, x, y, z \in \mathbb{N}, m > 2$ ) versus time during pyrolysis of TTIP<sub>130</sub> nanodroplet at 1500 K (Case 1 in Table 1) (a); 2000 K (Case 2 in Table 1) (b); and 2500 K (Case 3 in Table 1) (c). The normalization is performed in the way that  $\bar{n}$  represents the proportion of Ti element existing in a certain kind of species. The presented curves represent the averaged values of three independent runs with different initial configurations. Uncertainties of the simulation results are determined as the standard deviation of the three independent runs and are illustrated by the semi-transparent area around the curve.

flame with TTIP addition using an atmospheric pressure interface time-of-flight (APi-TOF) mass spectrometer. Pure  $\text{TiO}_2$  clusters were not detected by the authors and they argued that intermediates from TTIP decomposition might polymerize or aggregate into larger clusters prior to conversion to pure  $\text{TiO}_2$ .

Besides, Figs. 2(a), 2(b) and 2(c) show that temperature has a significant influence on the consumption rate of TTIP molecules. At 1500 K, TTIP molecules have not been fully consumed even at the end of simulation, although  $\sim 60\%$  of Ti elements have already participated in the formation of incipient Ti-containing clusters (i.e.,  $\text{Ti}_m\text{O}_x\text{C}_y\text{H}_z$  ( $m > 2$ ) species) by 6000 ps. In contrast, at a much higher pyrolysis temperature — 2500 K, the number of TTIP molecules decrease to 0 rapidly in less than 200 ps. Figure 2 also suggests that high temperature does not necessarily promotes the inception process of TTIP to Ti-containing clusters, as at 2500 K, only  $\sim 30\%$  Ti atoms are existed in the form of  $\text{Ti}_m\text{O}_x\text{C}_y\text{H}_z$ , which is much less than the percentage of Ti element existing in  $\text{Ti}_m\text{O}_x\text{C}_y\text{H}_z$  species at 1500 K and 2000 K. Since the peak concentrations of  $\text{Ti}_2\text{O}_x\text{C}_y\text{H}_z$  are similar at three temperatures, fewer  $\text{Ti}_m\text{O}_x\text{C}_y\text{H}_z$  during the 6000 ps simulation at 2500 K is supposed to be caused by the unstableness of Ti-O bonds at such high temperature. This can be reflected in Fig. 2(c) that the number of  $\text{Ti}_2\text{O}_x\text{C}_y\text{H}_z$  reduces quickly after reaching its peak value, which is accompanied by an instantaneous increase in the number of  $\text{TiO}_x\text{C}_y\text{H}_z$ , demonstrating the decomposition of the newly formed  $\text{Ti}_2\text{O}_x\text{C}_y\text{H}_z$  species, i.e., the breakup of the newly formed Ti-O bonds.

In order to explore the initial decomposition pathway of TTIP pyrolysis at different temperatures in a more detailed manner, we examined all of the Ti-containing species at the time when half of the TTIP molecules were consumed, i.e., the specific chemical formulas of  $\text{TiO}_x\text{C}_y\text{H}_z$  were inspected. Table 2 lists the number and the chemical formula of Ti-containing species at 806 ps of  $\text{TTIP}_{130}$  pyrolysis at 1500 K, corresponding to the state when 1/2 of initial TTIP molecules are consumed. Similar analysis was also performed for  $\text{TTIP}_{130}$  pyrolysis at 2000 K ( $t = 56.5$  ps) and 2500 K ( $t = 15.5$  ps), as shown by Tables S1 and S2. The possible formation pathway of these Ti-containing intermediate

species are also given in Tables 2, S1 and S2, based on the species information extracted every 0.5 ps during simulations.

Table 2: Chemical formulas of the Ti-containing intermediate species and their number at the time when 1/2 of initial TTIP molecules are consumed ( $t = 806$  ps) during TTIP<sub>130</sub> pyrolysis at 1500 K. Possible formation pathway is provided based on the species information extracted every 0.5 ps during MD simulations.

Species	Number	Formation pathway
TiO <sub>4</sub> C <sub>12</sub> H <sub>28</sub>	65	
TiO <sub>3</sub> C <sub>9</sub> H <sub>21</sub>	35	Ti-O break (-C <sub>3</sub> H <sub>7</sub> O)
TiO <sub>4</sub> C <sub>9</sub> H <sub>22</sub>	7	H shift; C-O break (-C <sub>3</sub> H <sub>6</sub> )
TiO <sub>3</sub> C <sub>6</sub> H <sub>15</sub>	5	Ti-O, C-O break (-2C <sub>3</sub> H <sub><i>x</i></sub> O <sub><i>y</i></sub> ) <sup>1</sup>
TiO <sub>3</sub> C <sub>6</sub> H <sub>14</sub>	4	Ti-O, C-O break (-2C <sub>3</sub> H <sub><i>x</i></sub> O <sub><i>y</i></sub> ) <sup>1</sup>
TiO <sub>2</sub> C <sub>6</sub> H <sub>14</sub>	3	2 Ti-O break (-2C <sub>3</sub> H <sub><i>x</i></sub> O <sub><i>y</i></sub> ) <sup>1</sup>
TiO <sub>4</sub> C <sub>9</sub> H <sub>21</sub>	3	C-O break (-C <sub>3</sub> H <sub>7</sub> )
TiO <sub>3</sub> C <sub>9</sub> H <sub>22</sub>	2	H shift; Ti-O break (-C <sub>3</sub> H <sub>6</sub> O)
TiO <sub>2</sub> C <sub>3</sub> H <sub>8</sub>	1	2 Ti-O, C-O break (-3C <sub>3</sub> H <sub><i>x</i></sub> O <sub><i>y</i></sub> ) <sup>1</sup>
TiO <sub>3</sub> C <sub>3</sub> H <sub>9</sub>	1	Ti-O, 2 C-O break (-3C <sub>3</sub> H <sub><i>x</i></sub> O <sub><i>y</i></sub> ) <sup>1</sup>
Ti <sub>2</sub> O <sub>5</sub> C <sub>15</sub> H <sub>35</sub>	1	
Ti <sub>2</sub> O <sub>5</sub> C <sub>12</sub> H <sub>29</sub>	1	

<sup>1</sup> When more than one Ti-O or C-O bonds are broken, it is hard to infer specific chemical formula of each released C/H/O-containing moieties, so  $x, y \in \mathbb{N}$  are used.

According to Tables 2, S1 and S2, the major products of initial decomposition of TTIP is TiO<sub>3</sub>C<sub>9</sub>H<sub>21</sub> at all three temperatures, which can be formed by breaking one Ti-O bond in a TTIP molecule; Meanwhile a C<sub>3</sub>H<sub>7</sub>O is released. The second most abundant Ti-containing intermediate species observed is TiO<sub>4</sub>C<sub>9</sub>H<sub>22</sub>. Since TiO<sub>4</sub>C<sub>9</sub>H<sub>22</sub> has four O atoms, it cannot be produced by Ti-O bond break, which will lead to the loss of O atoms. Based on analyzing the outputted species information and scrutinizing the simulated trajectory, we found TiO<sub>4</sub>C<sub>9</sub>H<sub>22</sub> was formed by break of one C-O bond in a TTIP molecule, prior to which an H atom shifts from C to O, thus C-O bond breaking results in

the release of one  $C_3H_6$  rather than  $C_3H_7$ . Generally, for a specific  $TiO_xC_yH_z$  species with  $x$ ,  $y$  and  $z$  known, its formation pathway can be inferred by comparing its number of O atoms (i.e.,  $x$ ) and C atoms (i.e.,  $y$ ) with those of a TTIP molecule ( $TiO_4C_{12}H_{28}$ ). Break of one Ti-O bond in a TTIP molecule will lead to loss of one O atom and three C atoms, while break of one C-O bond will remove three C atoms but the number of O atoms will not be affected. For pyrolysis at two higher temperatures, namely 2000 K and 2500 K, besides the break of Ti-O bonds and C-O bonds, break of C-C bonds is also observed. Break of one C-C bond in a TTIP molecule releases a  $CH_3$ , hence the number of C atoms in the resulted titanium intermediate species is no longer a multiple of 3.

It is also noteworthy that for  $TTIP_{130}$  pyrolysis at 1500 K,  $Ti_2O_xC_yH_z$  species already appear although only half of the TTIP molecules have been consumed at this time and no  $TiO_2$  molecule has been formed yet. To illustrate the formation pathway of the earliest/smallest Ti-containing clusters, i.e.,  $Ti_2O_xC_yH_z$  species, we tracked the evolution of the Ti atoms in  $Ti_2O_xC_yH_z$  species at 806 ps during  $TTIP_{130}$  pyrolysis at 1500 K. Take the formation of  $Ti_2O_5C_{12}H_{29}$  species as an example. Figure 3 illustrates how it is formed during  $TTIP_{130}$  pyrolysis at 1500 K. As highlighted by the dotted rectangular region

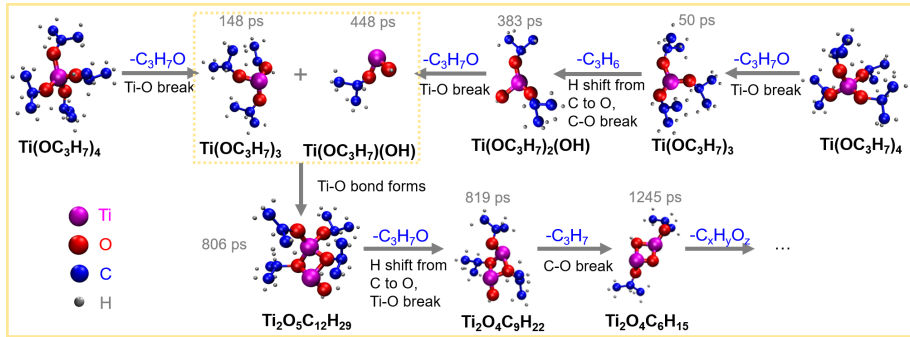
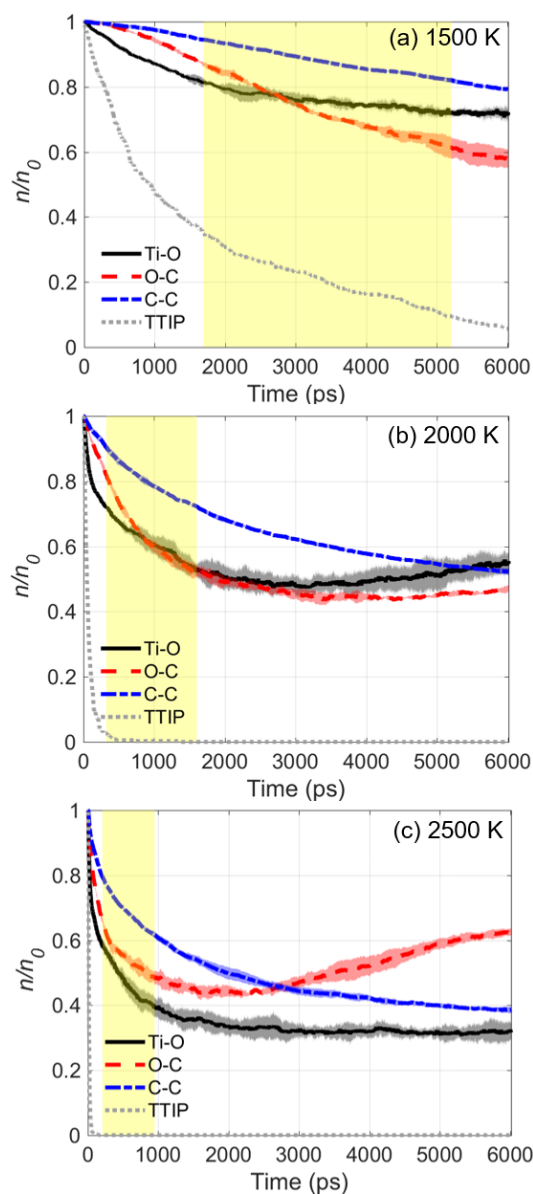


Figure 3: Illustration of the formation pathway of  $Ti_2O_5C_{12}H_{29}$  starting from two TTIP molecules (shown at the left and right side of the first row) during  $TTIP_{130}$  pyrolysis at 1500 K. Bonds between C atoms and H atoms are not shown for clarity. Corresponding simulation times of the snapshots are labeled on top in grey.

in Fig. 3,  $\text{Ti}_2\text{O}_5\text{C}_{12}\text{H}_{29}$  is formed by the combination of one  $\text{Ti}(\text{OC}_3\text{H}_7)_3$  and one  $\text{Ti}(\text{OC}_3\text{H}_7)(\text{OH})$ , both of which are intermediate titanium species converted from TTIP molecules. Break of one Ti-O bond in a TTIP molecule leads to  $\text{Ti}(\text{OC}_3\text{H}_7)_3$ , as shown by the upper left region in Fig. 3. The formation of  $\text{Ti}(\text{OC}_3\text{H}_7)(\text{OH})$  is demonstrated in the upper right region of Fig. 3. Starting from a TTIP molecule, at 50 ps, the break of one Ti-O bond in TTIP releases a  $\text{C}_3\text{H}_7\text{O}$  moiety and results in  $\text{Ti}(\text{OC}_3\text{H}_7)_3$ ; Next an H atom shifts from C atom to be bonded with O atom and then C-O bond breaks to release a  $\text{C}_3\text{H}_6$ , resulting in  $\text{Ti}(\text{OC}_3\text{H}_7)_2(\text{OH})$ ; After that another Ti-O bond breaks, leading to  $\text{Ti}(\text{OC}_3\text{H}_7)(\text{OH})$  until it combines with  $\text{Ti}(\text{OC}_3\text{H}_7)_3$  to form  $\text{Ti}_2\text{O}_5\text{C}_{12}\text{H}_{29}$ . The further evolution of  $\text{Ti}_2\text{O}_5\text{C}_{12}\text{H}_{29}$  after 806 ps is tracked for an extended period of time, which is shown the bottom row of Fig. 3. C atoms and H atoms in  $\text{Ti}_2\text{O}_5\text{C}_{12}\text{H}_{29}$  continue to be lost through break of Ti-O bonds and C-O bonds after 806 ps. This is reasonable as the target products using TTIP as precursors in flame reactors or hot wall flow reactors are  $\text{TiO}_2$  nanoparticles; Hydrocarbon components from the TTIP precursors are usually regarded as impurities that should be avoided.

After performing detailed examination on the initial decomposition (which typically finishes within 1000 ps under the simulated pyrolysis conditions in this work) pathway of TTIP molecules, we tracked the evolution of the number of Ti-O bonds, O-C bonds and C-C bonds during the entire 6000 ps simulation to obtain an overall picture of the bond evolution pattern during the pyrolysis of  $\text{TTIP}_{130}$ . The normalized number of Ti-O bonds, O-C bonds and C-C bonds in the simulation system versus time at three different pyrolysis temperatures, namely 1500 K, 2000 K and 2500 K, are displayed in Figs. 4(a), 4(b) and 4(c) respectively. The normalization is performed based on the initial number ( $n_0$ ) of a certain kind of bonds in the system, i.e., the number of Ti-O bonds and O-C bonds is normalized by  $130 \times 4 = 520$ , while the number of C-C bonds is normalized by  $130 \times 8 = 1040$ .

According to Figs. 4(a), 4(b) and 4(c), initially, the number of Ti-O bonds ( $n_{\text{b,Ti-O}}$ ) reduces faster than the number of O-C bonds ( $n_{\text{b,O-C}}$ ) with time



**Figure 4:** The normalized number of Ti-O bonds, O-C bonds, C-C bonds and TTIP molecules versus time during TTIP<sub>130</sub> pyrolysis at 1500 K (a); 2000 K (b); and 2500 K (c). The normalization factor  $n_0$  represents the initial number of a certain kind of bonds or TTIP molecules in the simulation system, i.e.,  $n_0 = 520$  for Ti-O bonds and O-C bonds;  $n_0 = 1040$  for C-C bonds;  $n_0 = 130$  for TTIP molecules. The presented curves represent the averaged values of three independent runs with different initial configurations. Uncertainties of the simulation results are determined as the standard deviation of three independent runs and are illustrated by the semi-transparent area around the curve. The semi-transparent yellow region denotes the time period when the number of  $\text{Ti}_2\text{O}_x\text{C}_y\text{H}_z$  species is larger than 1/2 of its peak value.

regardless of pyrolysis temperature, which agrees with our previous finding that break of Ti-O bonds in TTIP molecules is the most significant initial thermal decomposition pathway of TTIP followed by the break of O-C bonds (see Tables 2, S1 and S2). In addition, comparing with  $n_{b,Ti-O}$  and  $n_{b,O-C}$ , the decreasing rate of the number of C-C bonds ( $n_{b,C-C}$ ) is the smallest, which is consistent with the previous observation that the break of C-C bonds is much less frequent than the break of Ti-O bonds and O-C bonds (see Tables 2, S1 and S2). Comparison of Figs. 4(a), 4(b) and 4(c) indicates that fewest Ti-O, O-C, C-C bonds have been broken at 1500 K in 6000 ps, due to the much less reactivity of the system at 1500 K than that at two higher temperatures. For the time evolution of Ti-O bonds (shown by the black curve in Figs. 4(a), 4(b) and 4(c)), at the three pyrolysis temperatures,  $n_{b,Ti-O}$  decreases rather fast in the beginning, especially at the highest pyrolysis temperature — 2500 K, where the curve representing  $n_{b,Ti-O}$  is almost vertical within the first 100 ps of simulation. Then the decline rate of  $n_{b,Ti-O}$  gradually slows down as it enters the semi-transparent yellow region in Fig. 4, which denotes the time period during which the number of  $Ti_2O_xC_yH_z$  species is larger than 1/2 of its peak value. The formation of  $Ti_2O_xC_yH_z$  species means new Ti-O bonds are formed between two  $TiO_xC_yH_z$  species, thus it can offset the reduction of  $n_{b,Ti-O}$  caused by the break of Ti-O bonds in TTIP molecules to some extent. As indicated by Figs. 4(a) and 4(c), in 6000 ps pyrolysis simulation,  $\sim 30\%$  of the initial Ti-O bonds in TTIP molecules are broken at 1500 K, while the figure reaches  $\sim 70\%$  at 2500 K, which is equivalent to break of  $\sim 3$  Ti-O bonds in each TTIP molecule. Different trends of time evolution of  $n_{b,Ti-O}$  at three pyrolysis temperatures are also noteworthy. At 1500 K,  $n_{b,Ti-O}$  keeps decreasing during the 6000 ps simulation, although with a rather slow decline rate compared with that at 2000 K and 2500 K. At 2500 K,  $n_{b,Ti-O}$  decreases rapidly before 1000 ps, but after its value drops to  $\sim 0.3$ , it stops decreasing and becomes almost unchanged with time. At 2000 K,  $n_{b,Ti-O}$  first decreases but then gradually increases with time after around 3000 ps. The increase of  $n_{b,Ti-O}$  at 2000 K is supposed to be caused by the inception process, i.e., TTIP converting to Ti-containing clus-

ters, during which new Ti-O bonds can form between two titanium intermediate species. Based on the trend of time evolution of  $n_{b,Ti-O}$  in 6000 ps at 2500 K, it can be inferred that large Ti-containing clusters are almost unlikely to be formed under such condition because Ti-O bond formation is hardly observed after the initial break of Ti-O bonds in TTIP molecules. For amorphous  $TiO_2$  particles in a small size, the coordination number for Ti atoms is  $\sim 5$ , i.e., one Ti atom is bonded to five oxygen atoms [1, 51]. Therefore, if amorphous  $TiO_2$  nanoparticles are formed during simulation,  $n_{b,Ti-O}$  is expected to be near 1.25. However,  $n_{b,Ti-O}$  shown in Fig. 4 at all three pyrolysis temperatures are well below 1.25 at the end of the 6000 ps simulation, meaning most Ti atoms are still unsaturated.

Table 3 lists the Ti-containing clusters (i.e.,  $Ti_mO_xC_yH_z$ ,  $m \geq 4$ ) that have been formed at the end of 6000 ps pyrolysis simulation at 1500 K, 2000 K and 2500 K. O/Ti ratio of each species and the averaged O/Ti ratio of all  $Ti_mO_xC_yH_z$  species listed are also calculated. As demonstrated by Table 3, the observed Ti-containing clusters are rather small, the largest one (i.e.,  $Ti_{12}O_{13}H_5$  during pyrolysis at 1500 K) of which only consists of 12 Ti atoms, with gyration diameter less than 1 nm ( $\sim 5.8 \text{ \AA}$ ). In addition, these incipient titanium clusters, i.e.,  $Ti_mO_xC_yH_z$  species, are highly unsaturated in terms of O/Ti ratio. Ti-containing clusters formed through 1500 K pyrolysis have the largest averaged O/Ti ratio – 1.18, among the three pyrolysis temperature, which is still well below 2 – the value expected in  $TiO_2$  nanoparticles. At 2500 K, the average O/Ti ratio drops to only  $\sim 0.9$ .

It is worth mentioning that although most  $Ti_mO_xC_yH_z$  ( $m \geq 4$ ) species are formed at the lowest pyrolysis temperature, namely 1500 K, these incipient Ti-containing clusters can contain a certain amount of carbon impurities, as suggested by the lower part of Table 3. By contrast, at the highest pyrolysis temperature simulated in this work, i.e., 2500 K, no carbon impurities are observed in the incipient Ti-containing clusters, which however, is on the expense of much fewer  $Ti_mO_xC_yH_z$  species being formed at such high temperature. This may suggest that if TTIP were used as precursors to produce  $TiO_2$  nanoparti-

Table 3: The number of  $\text{Ti}_m\text{O}_x\text{C}_y\text{H}_z$  ( $m, x, y, z \in \mathbb{N}, m \geq 4$ ) species and their corresponding O/Ti ratio at the end of the 6000 ps simulation of TTIP<sub>130</sub> nanodroplet pyrolysis at 1500 K, 2000 K and 2500 K.

$T = 1500 \text{ K}$			$T = 2000 \text{ K}$			$T = 2500 \text{ K}$		
Species	$n$	O/Ti	Species	$n$	O/Ti	Species	$n$	O/Ti
$\text{Ti}_{12}\text{O}_{13}\text{H}_5$	1	1.08	$\text{Ti}_7\text{O}_7\text{H}$	1	1.00	$\text{Ti}_{11}\text{O}_8$	1	0.73
$\text{Ti}_{11}\text{O}_{12}\text{H}_4$	1	1.09	$\text{Ti}_7\text{O}_7$	5	1.00	$\text{Ti}_9\text{O}_8$	1	0.89
$\text{Ti}_8\text{O}_8\text{H}$	1	1.00	$\text{Ti}_7\text{O}_6\text{H}$	1	0.86	$\text{Ti}_9\text{O}_7$	1	0.78
$\text{Ti}_7\text{O}_8\text{H}_2$	3	1.14	$\text{Ti}_7\text{O}_6$	2	0.86	$\text{Ti}_8\text{O}_7$	1	0.88
$\text{Ti}_7\text{O}_8\text{H}$	1	1.14	$\text{Ti}_6\text{O}_6\text{H}$	1	1.00	$\text{Ti}_6\text{O}_5$	1	0.83
$\text{Ti}_7\text{O}_7\text{H}_2$	1	1.00	$\text{Ti}_6\text{O}_6$	6	1.00	$\text{Ti}_5\text{O}_5$	2	1.00
$\text{Ti}_7\text{O}_7$	1	1.00	$\text{Ti}_5\text{O}_6\text{H}_3$	1	1.20	$\text{Ti}_4\text{O}_5\text{H}_2$	1	1.25
$\text{Ti}_6\text{O}_7\text{H}_4$	1	1.17	$\text{Ti}_5\text{O}_6\text{H}_2$	1	1.20	$\text{Ti}_4\text{O}_4$	9	1.00
$\text{Ti}_5\text{O}_6\text{H}_2$	1	1.20	$\text{Ti}_5\text{O}_5\text{H}$	5	1.00	$\text{Ti}_4\text{O}_3$	2	0.75
$\text{Ti}_5\text{O}_6\text{H}$	1	1.20	$\text{Ti}_5\text{O}_5$	1	1.00			
$\text{Ti}_4\text{O}_6\text{H}_5$	1	1.50	$\text{Ti}_5\text{O}_4$	2	0.80			
$\text{Ti}_4\text{O}_5\text{H}_3$	1	1.25	$\text{Ti}_4\text{O}_4\text{H}$	1	1.00			
$\text{Ti}_4\text{O}_5\text{H}_2$	1	1.25	$\text{Ti}_4\text{O}_4$	21	1.00			
$\text{Ti}_4\text{O}_5\text{H}$	1	1.25	$\text{Ti}_4\text{O}_3$	1	0.75			
$\text{Ti}_4\text{O}_4\text{H}$	2	1.00						
$\text{Ti}_4\text{O}_4$	7	1.00						
$\text{Ti}_{12}\text{O}_{16}\text{C}_6\text{H}_{19}$	1	1.33	$\text{Ti}_5\text{O}_4\text{C}_2\text{H}_2$	1	0.80			
$\text{Ti}_7\text{O}_{11}\text{C}_2\text{H}_{10}$	1	1.57						
$\text{Ti}_7\text{O}_9\text{C}_6\text{H}_{18}$	1	1.29						
$\text{Ti}_6\text{O}_9\text{C}_6\text{H}_{16}$	1	1.50						
$\text{Ti}_5\text{O}_6\text{C}_6\text{H}_{15}$	1	1.20						
$\text{Ti}_4\text{O}_7\text{C}_6\text{H}_{16}$	1	1.75						
$\text{Ti}_4\text{O}_6\text{C}_6\text{H}_{15}$	1	1.50						
$\text{Ti}_4\text{O}_5\text{C}_3\text{H}_6$	1	1.25						
Avg. O/Ti ratio		1.18			0.98			0.91

<sup>1</sup> Results are based on three independent runs with different initial configurations at each temperature. Species listed in the lower part of the table contain carbon components, i.e.,  $y > 0$

cles through pyrolysis, the optimal reactor temperature needs to be determined in order to obtain a satisfactory production rate as well as the lowest amount of carbon impurities. Another interesting finding based on Table 3 is that  $\text{Ti}_4\text{O}_4$  is found to be an important Ti-containing intermediate species during the pyrolysis of TTIP, as its number is notably higher than other titanium species regardless of temperature. We noticed that  $\text{Ti}_4\text{O}_4$  has a cube molecular structure, with four Ti atoms and four O atoms alternatively distributed on the vertex of a cube (Illustration of the molecular structure of  $\text{Ti}_4\text{O}_4$  can be found in the snapshots of Fig. 5), making it quite stable even at temperatures higher than 2000 K.

To illustrate the growth pathway of Ti-containing clusters during the pyrolysis of  $\text{TTIP}_{130}$ , we tracked the formation pathway of the largest Ti-containing cluster observed in the simulation, i.e.,  $\text{Ti}_{12}\text{O}_{13}\text{H}_5$ . Figure 5 shows its growth path starting from  $\text{Ti}_4\text{O}_4$ . The first row and second row in Fig. 5 illustrate how

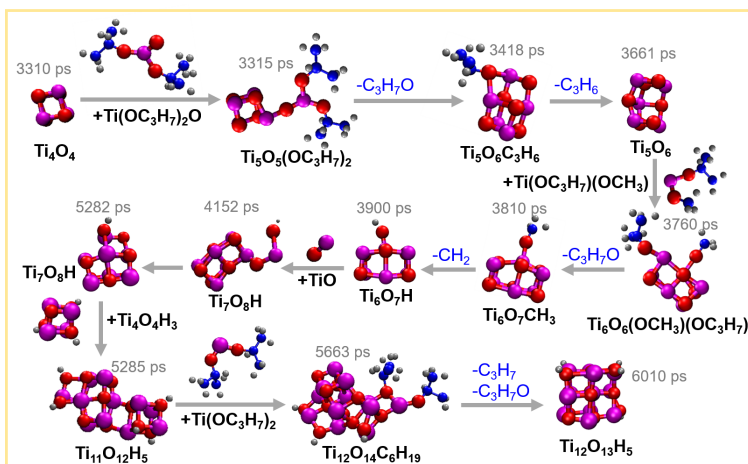
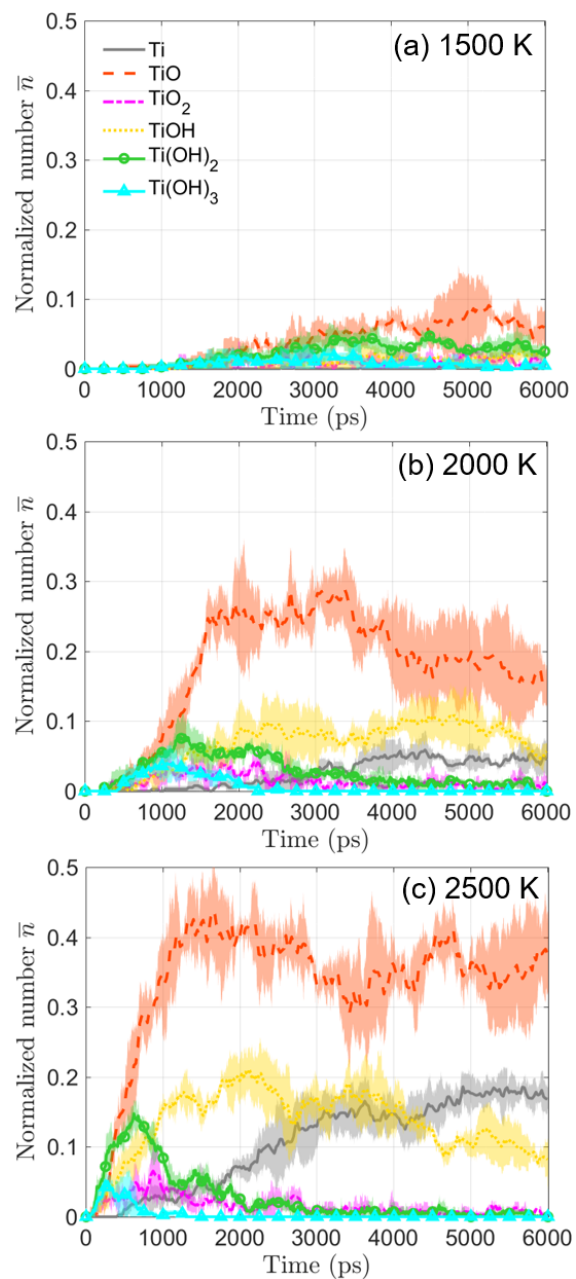


Figure 5: Illustration of the formation pathway of  $\text{Ti}_{12}\text{O}_{13}\text{H}_5$  starting from  $\text{Ti}_4\text{O}_4$  during  $\text{TTIP}_{130}$  pyrolysis at 1500 K. Corresponding simulation times of the snapshots are labeled beside in grey. Magenta, red, blue and silver represent Ti, O, C and H atoms, respectively.

$\text{Ti}_4\text{O}_4$  has grown up to  $\text{Ti}_7\text{O}_8\text{H}$ . Briefly,  $\text{Ti}_4\text{O}_4$  has combined with a series of Ti-containing intermediate species including  $\text{Ti}(\text{OC}_3\text{H}_7)_2\text{O}$ ,  $\text{Ti}(\text{OC}_3\text{H}_7)(\text{OCH}_3)$  and  $\text{TiO}$  through formation of Ti-O bonds. Meanwhile, it keeps releasing some

hydrocarbon moieties such as  $C_3H_7O$ ,  $C_3H_6$  and  $CH_2$  through breaking of Ti-O bonds and C-O bonds. At 5285 ps, the collision between  $Ti_7O_8H$  and  $Ti_4O_4H_3$  leads to the formation of a larger titanium cluster, i.e.,  $Ti_{11}O_{12}H_5$ , which is illustrated at the beginning of the third row in Fig. 5. After then,  $Ti(OC_3H_7)_2$  is bonded to  $Ti_{11}O_{12}H_5$ , resulting in  $Ti_{12}O_{14}C_6H_{19}$ . Later on,  $C_3H_7$  and  $C_3H_7O$  are released from  $Ti_{12}O_{14}C_6H_{19}$  through the break of Ti-O bond and C-O bond, leading to the formation of  $Ti_{12}O_{13}H_5$  finally.

Since Fig. 2 shows that the concentration of  $TiO_2$  is rather low during pyrolysis of  $TTIP_{130}$ , we then identified the major Ti-containing intermediate species based on the obtained simulation results. Figures 6(a), 6(b) and 6(c) illustrate the normalized number  $\bar{n}$  of Ti, TiO,  $TiO_2$ , TiOH,  $Ti(OH)_2$  and  $Ti(OH)_3$  versus time during  $TTIP_{130}$  pyrolysis at 1500 K, 2000 K and 2500 K, respectively. It can be seen in Fig. 6 that at 1500 K, the number of all these six species are much lower than those at 2000 K and 2500 K. This is because at 1500 K, most of Ti element ends up in forming larger titanium clusters, i.e.,  $Ti_mO_xC_yH_z$  ( $m > 1$ ) species rather than existing in the form of  $TiO_xC_yH_z$ , which has been illustrated in Fig. 2(a). Figure 6 also shows that comparing with  $TiO_2$ , the number of TiO species is more significant at all three pyrolysis temperatures, especially at 2500 K, where more than 40% of Ti element exists in TiO. Besides TiO, other three species, namely  $Ti(OH)_2$ , TiOH and Ti are also found to be non-negligible at 2000 K and 2500 K. According to Figs. 6(b) and 6(c),  $Ti(OH)_2$  is accumulated with time at first; After reaching its peak concentration, i.e.,  $\bar{n}_{\max, Ti(OH)_2} \approx 0.1$  at 2000 K and  $\bar{n}_{\max, Ti(OH)_2} \approx 0.15$  at 2500 K, its number begins to decrease with time, meaning it is being consumed. This suggests that  $Ti(OH)_2$  serves as a key intermediate species during the pyrolysis of  $TTIP$ . In contrast,  $Ti(OH)_4$ , which was considered to be the most important intermediate species along the pathway of  $TTIP$  conversion to  $TiO_2$  [24, 33, 41, 72–74], however, is found to be negligible at all three pyrolysis temperatures and thus is not shown in Fig. 6. Although  $Ti(OH)_4$  is rather insignificant, a small amount of  $Ti(OH)_3$  is observed as demonstrated by the cyan curve in Fig. 6. Based on the trends of the time evolution of  $Ti(OH)_3$ ,  $Ti(OH)_2$  and TiOH displayed in Figs. 6(b) and



**Figure 6:** Normalized number  $\bar{n}$  of Ti, TiO, TiO<sub>2</sub>, TiOH, Ti(OH)<sub>2</sub> and Ti(OH)<sub>3</sub> versus time during TTIP<sub>130</sub> pyrolysis at 1500 K (a); 2000 K (b); and 2500 K (c). The normalization is performed in the way that  $\bar{n}$  represents the proportion of Ti element existing in the form of a certain species. The presented curves represent the averaged values of three independent runs with different initial configurations. Uncertainties of the simulation results are determined as the standard deviation of three independent runs and are illustrated by the semi-transparent area around the curve.

Fig. 6(c), the relationship among these three Ti-containing intermediate species may be inferred as  $\text{Ti}(\text{OH})_3 \rightarrow \text{Ti}(\text{OH})_2 \rightarrow \text{TiOH}$  through continuous breaking of Ti-O bonds at high-temperature environment. The reason why  $\text{Ti}(\text{OH})_4$  is hardly observed can be attributed to the relatively high pyrolysis temperatures ( $T \geq 1500$  K) used in our simulations. According to Buerger et al. [23],  $\text{Ti}(\text{OH})_4$  was the most stable titanium species when  $T < 1250$  K. Our simulation results shown in Fig. 6 suggests that the previous decomposition mechanism of TTIP which regarded  $\text{Ti}(\text{OH})_4$  as the most important intermediate titanium species before formation of  $\text{TiO}_2$  needs to be re-examined in future work, at least for the high-temperature regime of  $T \geq 1500$  K.

To the best of the authors' knowledge, experimental data measuring the intermediate titanium species during TTIP pyrolysis at temperatures higher than 1500 K has rarely been reported. The most relevant experimental study investigating the elementary TTIP decomposition mechanism we could find in literature was performed by Ershov et al. [40], who conducted UV-Photodissociation experiments on TTIP and detected the photofragments using the time-of-flight mass spectrometer (TOF-MS) technique. Ti and TiO were found to be the most abundant photofragments based on their measurements, which agrees well with our simulation results on the thermal decomposition of TTIP at 2500 K (see Fig. 6(c)).

### 3.2. Combustion of $\text{TTIP}_{130}$ with $\text{O}_2$ – Effect of $\text{O}_2$ concentration

In the previous section, the inception process of TTIP conversion to incipient Ti-containing clusters has been examined in detail. In this section, the effect of  $\text{O}_2$  on the inception mechanism of TTIP to titanium clusters will be investigated, because  $\text{O}_2$  is the most common oxidizer in flame reactors and is often used as dispersion gas to atomize the liquid precursor in nanoparticle synthesis through FSP [13, 20].

Figure 7 shows the time evolution of the normalized number  $\bar{n}$  of TTIP,  $\text{O}_2$ ,  $\text{TiO}_2$ ,  $\text{TiO}_x\text{C}_y\text{H}_z$ ,  $\text{Ti}_2\text{O}_x\text{C}_y\text{H}_z$  and  $\text{Ti}_m\text{O}_x\text{C}_y\text{H}_z$  ( $m, x, y, z \in \mathbb{N}, m > 2$ ) during  $\text{TTIP}_{130}$  reacting with 2340  $\text{O}_2$  molecules at 2500 K. Comparing the

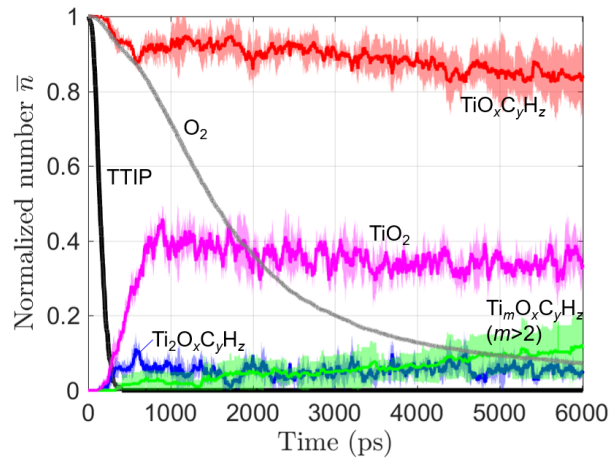
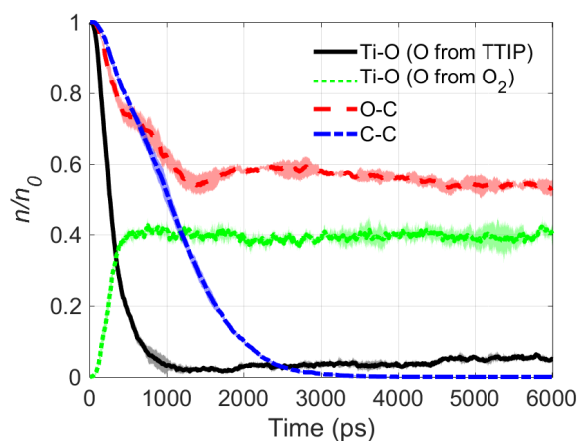


Figure 7: Normalized number  $\bar{n}$  of TTIP,  $O_2$ ,  $TiO_2$ ,  $TiO_xC_yH_z$ ,  $Ti_2O_xC_yH_z$  and  $Ti_mO_xC_yH_z$  ( $m > 2$ ) versus time during TTIP<sub>130</sub> reacting with 2340  $O_2$  molecules at 2500 K (i.e., Case 4 in Table 1). For Ti-containing species, the normalization is performed in the way that  $\bar{n}$  represents the proportion of Ti element existing in a certain kind of species. For  $O_2$ , the normalization factor is its initial number  $n_0 = 2340$ . The presented curves represent the averaged values of three independent runs with different initial configurations. Uncertainties of the simulation results are determined as the standard deviation of three independent runs and are illustrated by the semi-transparent area around the curve.

curves shown in Fig. 7 with those obtained during TTIP<sub>130</sub> pyrolysis at 2500 K without surrounding O<sub>2</sub> molecules (Fig. 2(c)) can demonstrate the effect of O<sub>2</sub> addition on the time evolution of these key species. It is found that the time evolution of  $\bar{n}$  of TiO<sub>x</sub>C<sub>y</sub>H<sub>z</sub>, Ti<sub>2</sub>O<sub>x</sub>C<sub>y</sub>H<sub>z</sub> and Ti<sub>m</sub>O<sub>x</sub>C<sub>y</sub>H<sub>z</sub> ( $m > 2$ ) species show similar pattern regardless of O<sub>2</sub>. However, with O<sub>2</sub> introduced in the simulation system, a significant increase in the amount of TiO<sub>2</sub> is observed. Not only TiO<sub>2</sub> takes up ~40% of Ti element with O<sub>2</sub> addition, but it also appears earlier than Ti<sub>2</sub>O<sub>x</sub>C<sub>y</sub>H<sub>z</sub> species, which is contrary to the simulation results of TTIP<sub>130</sub> pyrolysis at 2500 K illustrated in Fig. 2(c). This is interesting because with O<sub>2</sub> introduced, the simulation results seem to be more in line with the previous understanding on the inception mechanism of TTIP to TiO<sub>2</sub> nanoparticles, which believed that TTIP was first converted to TiO<sub>2</sub> vapors followed by homogeneous nucleation when TiO<sub>2</sub> vapors were sufficiently supersaturated [17].

We then examined the time evolution of Ti-O bonds, O-C bonds and C-C bonds during the entire 6000 ps simulation of TTIP<sub>130</sub> reacting with 2340 O<sub>2</sub> molecules. To demonstrate the role played by O<sub>2</sub>, Ti-O bonds in the simulation system are classified into two categories based on the origin of O atoms in a Ti-O bond. Initially, there are 520 Ti-O bonds in the system, where all O atoms come from TTIP. However, as chemical reactions proceed in the system, original Ti-O bonds can break and new Ti-O bonds can form between Ti atoms and O atoms from gaseous O<sub>2</sub> molecules. Figure 8 illustrates the normalized number of Ti-O bonds ( $n_{b,Ti-O(TTIP)}$  and  $n_{b,Ti-O(O_2)}$  for O atom in Ti-O bond from TTIP and O<sub>2</sub> respectively), O-C bonds ( $n_{b,O-C}$ ) and C-C bonds ( $n_{b,C-C}$ ) versus simulation time. Comparing the time evolution of  $n_{b,Ti-O(TTIP)}$  when TTIP<sub>130</sub> is surrounded by 2340 O<sub>2</sub> molecules with that of  $n_{b,Ti-O}$  during TTIP<sub>130</sub> pyrolysis at 2500 K shown in Fig. 2(c), it is evident that addition of O<sub>2</sub> has significantly promoted the break of Ti-O bonds in TTIP. In Fig. 2(c), ~70% of initial Ti-O bonds in TTIP molecules have broken in 6000 ps, while as suggested by Fig. 8, almost all of the original Ti-O bonds are broken. While the original Ti-O bonds are broken, new Ti-O bonds between Ti atoms and O atoms from O<sub>2</sub> molecules



**Figure 8:** The normalized number of Ti-O bonds (O atom from TTIP), Ti-O bonds (O atom from gaseous O<sub>2</sub>), O-C bonds and C-C bonds versus time during TTIP<sub>130</sub> reacting 2340 O<sub>2</sub> at 2500 K. The normalization factor  $n_0$  represents the initial number of a certain kind of bonds in the simulation system, i.e.,  $n_0 = 520$  for Ti-O bonds and O-C bonds;  $n_0 = 1040$  for C-C bonds. The presented curves represent the averaged values of three independent runs with different initial configurations. Uncertainties of the simulation results are determined as the standard deviation of three independent runs and are illustrated by the semi-transparent area around the curve.

are constantly being formed till  $n_{b,Ti-O(O_2)}$  achieves  $\sim 0.4$  (at around 500 ps). This is equivalent to that on average, each Ti atom is bonded with 1.6 O atoms from  $O_2$ , while almost all of the four original Ti-O bonds in TTIP molecules are broken. Briefly, Fig. 8 is suggesting that when gaseous  $O_2$  molecules are introduced, O atoms in  $O_2$  will replace the original O atoms in TTIP to form new Ti-O bonds.

To identify the major titanium intermediate species during  $TTIP_{130}$  reacting with 2340  $O_2$  molecules, the time evolution of eight Ti/O/H-containing species are examined and the results are plotted in Fig. 9. As suggested by Fig. 9, TiO

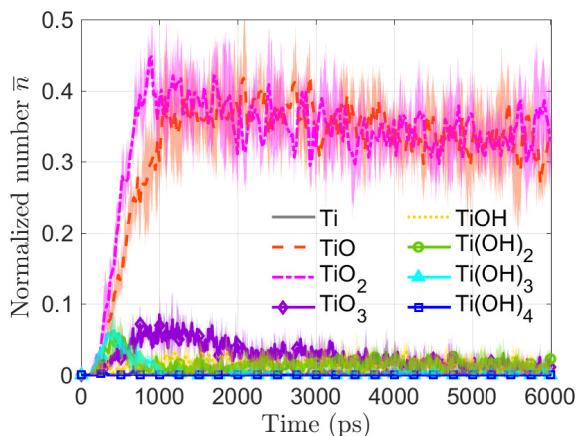


**Figure 9:** The normalized number  $\bar{n}$  of Ti, TiO,  $TiO_2$ ,  $TiO_3$ , TiOH,  $Ti(OH)_2$ ,  $Ti(OH)_3$  and  $Ti(OH)_4$  versus time during  $TTIP_{130}$  reacting with 2340  $O_2$  molecules at 2500 K. The normalization is performed in the way that  $\bar{n}$  represents the proportion of Ti element existing in the form of a certain species. The presented curves represent the averaged values of three independent runs with different initial configurations. Uncertainties of the simulation results are determined as the standard deviation of three independent runs and are illustrated by the semi-transparent area around the curve.

and  $TiO_2$  are found to be two most dominant titanium intermediate species when  $TTIP_{130}$  is reacting with 2340  $O_2$  molecules at 2500 K. Almost  $\sim 80\%$  of Ti element exists in these two species, with each of them taking up  $\sim 40\%$  of the total Ti element. Comparing with the pyrolysis case at 2500 K, i.e., Case 3 in Table 1, it can be seen that the amount of TiO is similar (see Fig. 6(c)), i.e.,

$\bar{n}_{\text{TiO}} \approx 0.4$  whether  $\text{O}_2$  is introduced or not. Similar to the pyrolysis case at 2500 K,  $\text{Ti}(\text{OH})_4$  also appears to be negligible in Case 4. Atomic Ti is hardly detected with  $\text{O}_2$  addition in Case 4, which is understandable because it tends to be oxidized by the sufficient  $\text{O}_2$  molecules in the simulation system, leading to various titanium oxides including TiO,  $\text{TiO}_2$  and even a small amount of  $\text{TiO}_3$ .

Figure 10 illustrates the typical formation pathway of TiO and  $\text{TiO}_2$  in Case 4 (i.e.,  $\text{TTIP}_{130}$  reacting with 2340  $\text{O}_2$  molecules at 2500 K), which are the two most dominant titanium species that are formed in Case 4. It also clearly demon-

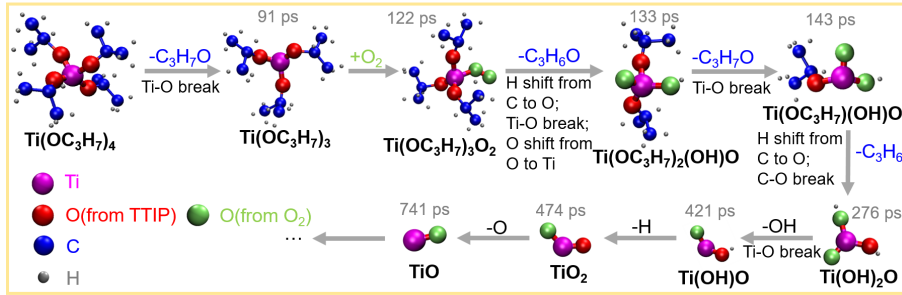
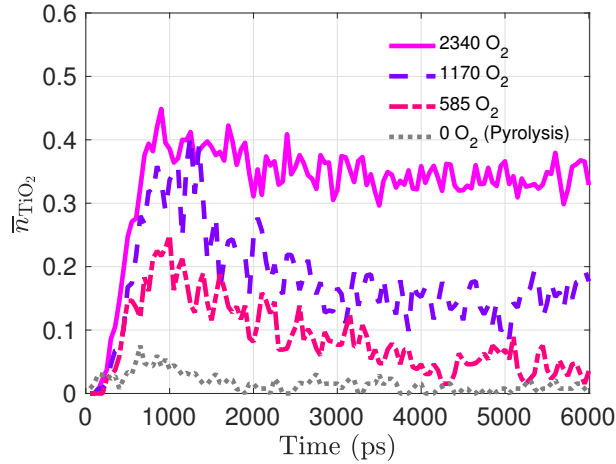


Figure 10: Illustration of the formation pathway of TiO and  $\text{TiO}_2$  starting from a TTIP molecule during  $\text{TTIP}_{130}$  reacting with 2340  $\text{O}_2$  at 2500 K (i.e., Case 4 in Table 1). Corresponding simulation times of the snapshots are labeled beside in grey.

strates how O atoms in  $\text{O}_2$  molecules has replaced the original O atoms in TTIP gradually. As illustrated by Fig. 10, the whole reaction is initiated by the break of a Ti-O bond in a TTIP molecule, which releases a  $\text{C}_3\text{H}_7\text{O}$  and a  $\text{Ti}(\text{OC}_3\text{H}_7)_3$  is formed. This initiation process is similar to that in the pyrolysis case (see Fig. 3). Since Ti atom in  $\text{Ti}(\text{OC}_3\text{H}_7)_3$  is unsaturated, an  $\text{O}_2$  molecule comes to bond with it thus forming  $\text{Ti}(\text{OC}_3\text{H}_7)_3\text{O}_2$ . Then a  $\text{C}_3\text{H}_6\text{O}$  is released through the break of another Ti-O bond, leading to  $\text{Ti}(\text{OC}_3\text{H}_7)_2(\text{OH})\text{O}$ . At 133 ps, in  $\text{Ti}(\text{OC}_3\text{H}_7)_2(\text{OH})\text{O}$ , both O atoms from  $\text{O}_2$  are bonded with the Ti atom, as this configuration should have the lowest potential energy. So far, two atoms in a gaseous  $\text{O}_2$  has successfully replaced two original O atoms in TTIP. Following reactions show similar patterns as those observed in the pyrolysis case (see Fig.

3). Hydrocarbon moieties such as  $C_3H_7O$  and  $C_3H_6$  are released by break of Ti-O bond or C-O bond. Due to the high simulation temperature, i.e., 2500 K, Ti-O bond keeps breaking after the titanium species becomes carbon-free. This is illustrated by the second row of Fig. 10, demonstrating the conversion of  $Ti(OH)_2O \rightarrow Ti(OH)O \rightarrow TiO_2 \rightarrow TiO$  through continuous breaking of two Ti-O bonds.

To investigate the effect of different concentration of  $O_2$  on the inception process of TTIP conversion to incipient clusters, besides introducing 2340  $O_2$  molecules in the simulation system (i.e., Case 4), we performed two more simulations of  $TTIP_{130}$  reacting with 1170  $O_2$  (i.e., Case 5) and 585  $O_2$  molecules (i.e., Case 6) at 2500 K, respectively. Figure 11 shows the normalized number



**Figure 11:** The normalized number of  $TiO_2$  versus time during  $TTIP_{130}$  reacting with 2340  $O_2$  molecules (Case 4), 1170  $O_2$  molecules (Case 5), 585  $O_2$  molecules (Case 6) and 0  $O_2$  (i.e., pyrolysis; Case 3) at 2500 K, respectively.  $\bar{n}_{TiO_2}$  represents the proportion of Ti element existing in  $TiO_2$ , i.e.,  $\bar{n}_{TiO_2} = n_{TiO_2}/130$ .

of  $TiO_2$  ( $\bar{n}_{TiO_2}$ ) versus time during  $TTIP_{130}$  reacting with different numbers of  $O_2$  molecules, i.e., different concentrations of  $O_2$ , at 2500K. For comparison, the time evolution of  $\bar{n}_{TiO_2}$  during  $TTIP_{130}$  pyrolysis at 2500 K is also shown in Fig. 11, which represents the extreme condition without any  $O_2$ . Figure 11 suggests the amount of produced  $TiO_2$  increases with increasing  $O_2$  concentra-

tion. While for other key intermediate titanium species including  $\text{TiO}_x\text{C}_y\text{H}_z$ ,  $\text{Ti}_2\text{O}_x\text{C}_y\text{H}_z$  and  $\text{Ti}_m\text{C}_x\text{H}_y\text{O}_z$  ( $m > 2$ ), their time evolutions exhibit parallel patterns regardless of  $\text{O}_2$  concentration, thus are not shown here. Since the concentration of  $\text{O}_2$  can significantly influence the amount of  $\text{TiO}_2$ , it indicates that enough  $\text{O}_2$  supply is important to convert TTIP precursors to  $\text{TiO}_2$  vapors in FSP.

### 3.3. Combustion of $\text{TTIP}_{130}$ with $\text{O}_2$ – Effect of high-temperature residence time

High-temperature residence time measures how long particles have been in the high-temperature region in the flame, i.e., it represents the temperature-time history of the flame-generated particles [13]. It is an important factor in flame synthesis of nanomaterials because temperature gradient in flames can be quite steep and it can vary by changing flame conditions such as changing the fuel/oxidizer flow rate, adjusting the height of the stagnation plate, etc.

To explore the effect of high-temperature residence time on the inception process of TTIP, we imposed five different temperature profiles (shown in Fig. 12(a)) to perform simulations of  $\text{TTIP}_{130}$  reacting with 2340  $\text{O}_2$  molecules. The upper and lower limits of the five created temperature profiles are chosen to be 2500 K and 1000 K, respectively, based on the flame temperature measured in the FSP experiments conducted by Madler et al. [13]. In Fig. 12(a), the area enclosed by the temperature curve and the axes reflects the temperature-time history, i.e., high-temperature residence time. Hence, the sequence of  $T_4 < T_5 < T_1 < T_2 < T_3$  can be obtained if these five temperature profiles are sorted according to high-temperature residence time.

Figure 12(b) illustrates the time evolution of the normalized number of  $\text{TiO}_2$  molecules under five different temperature profiles. For comparison, the results of Case 4 in which  $T$  is controlled to 2500 K in the whole 6000 ps simulation is also plotted in Fig. 12(b). For all cases shown in Fig. 12(b),  $\bar{n}_{\text{TiO}_2}$  achieves its maximum value during 1000 ps–2000 ps, with  $\sim 40\%$  of Ti element from TTIP being converted to  $\text{TiO}_2$  molecules. After then, the trend of  $\bar{n}_{\text{TiO}_2}$  becomes different from each other, depending on the temperature profile being

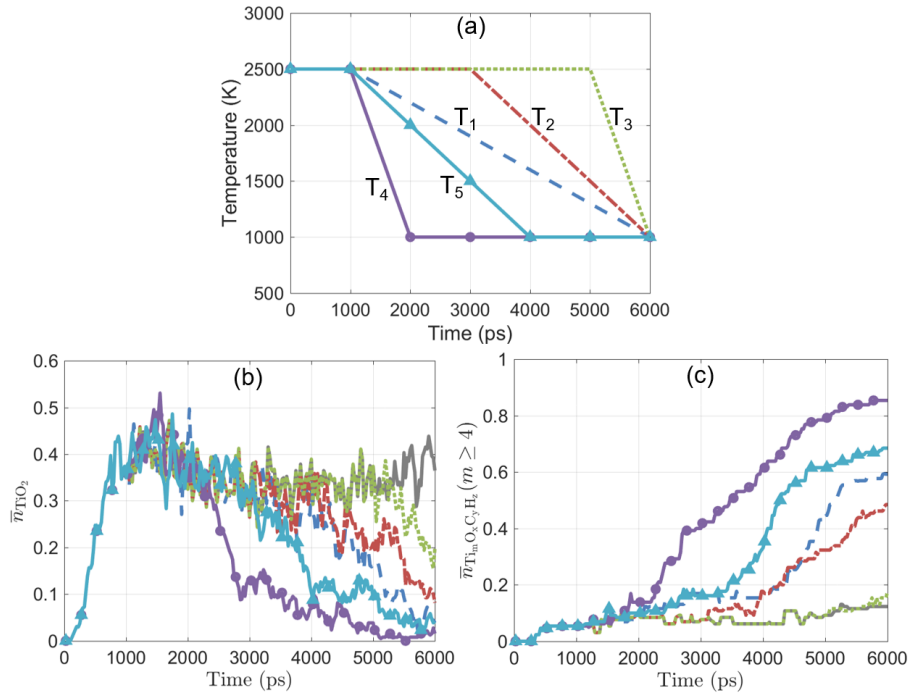


**Figure 12:** Five temperature profiles  $T_1$ ,  $T_2$ ,  $T_3$ ,  $T_4$  and  $T_5$  that are imposed for simulation Cases 7, 8, 9, 10 and 11, respectively (a); Normalized number of  $\text{TiO}_2$  molecules (b) and  $\text{Ti}_m\text{O}_xC_y\text{H}_z$  ( $m \geq 4$ ) species with different temperature profiles  $T_1 - T_5$  being imposed (i.e., Cases 7, 8, 9, 10, 11) during simulation versus time. The grey curves in (b) and (c) represent the results obtained at  $T = 2500$  K (i.e., Case 4). The normalization is performed in the way that  $\bar{n}$  represents the proportion of Ti element existing in  $\text{TiO}_2$  and in  $\text{Ti}_m\text{O}_xC_y\text{H}_z$  ( $m \geq 4$ ).

imposed for simulation. Among the five imposed temperature profiles,  $\bar{n}_{\text{TiO}_2}$  obtained with  $T_4$  profile sees the most significant reduction versus time, while  $\bar{n}_{\text{TiO}_2}$  obtained with  $T_4$  profile sees the most insignificant decrease against time. By contrast, almost no decline of  $\bar{n}_{\text{TiO}_2}$  is observed for Case 4, in which the temperature is kept at 2500 K through entire 6000 ps simulation. Figure 12(c) suggests that the amount of  $\text{Ti}_m\text{O}_x\text{C}_y\text{H}_z$  ( $m \geq 4$ ) species increases with decreasing high-temperature residence time.  $T_4$  profile corresponds to the shortest high-temperature residence time yet sees the most significant formation of  $\text{Ti}_m\text{O}_x\text{C}_y\text{H}_z$  species. This can be explained as the relatively low temperature after 1000 ps promotes the condensation process of  $\text{TiO}_2$  vapors formed before  $\sim 1000$  ps, because the saturated vapor pressure of  $\text{TiO}_2$  decreases with decreasing temperature. Condensation of  $\text{TiO}_2$  vapors leads to formation of  $\text{Ti}_m\text{O}_x\text{C}_y\text{H}_z$  species, as the decrease of  $\text{TiO}_2$  shown in Fig. 12(b) and the increase of  $\text{Ti}_m\text{O}_x\text{C}_y\text{H}_z$  species shown in Fig. 12(c) echo each other.

Since Fig. 12(c) indicates significantly promoted formation of  $\text{Ti}_m\text{O}_x\text{C}_y\text{H}_z$  ( $m \geq 4$ ) species with decreased high-temperature residence time, a closer examination was then taken on these incipient Ti-containing clusters under various temperature profiles. Table 4 lists the chemical formulas of  $\text{Ti}_m\text{O}_x\text{C}_y\text{H}_z$  ( $m > 4$ ) species that have been formed at the end of 6000 ps simulation of TTIP<sub>130</sub> reacting with 2340  $\text{O}_2$  molecules under different temperature profiles. The largest species in terms of the number of Ti atoms and O atoms listed in Table 4 is  $\text{Ti}_{20}\text{O}_{47}\text{C}_3\text{H}_{16}$ , which is obtained with the shortest high-temperature residence time being imposed in simulation, i.e.,  $T_4$  temperature profile. The average O/Ti ratio and C/Ti ratio of the incipient Ti-containing clusters obtained with different high-temperature residence time are also calculated and listed in Table 4. The average O/Ti ratio of  $\text{Ti}_m\text{O}_x\text{C}_y\text{H}_z$  ( $m \geq 4$ ) species is 1.18 for Case 4, which is slightly higher than the value calculated for Case 3, i.e., TTIP<sub>130</sub> pyrolysis at 2500 K without  $\text{O}_2$  addition (O/Ti = 0.91, see Table 3). The amount of  $\text{Ti}_m\text{O}_x\text{C}_y\text{H}_z$  ( $m \geq 4$ ) species in both Case 3 and Case 4 are rather few, as Ti-O bonds are not stable at such high temperature. For cases in which cooling stage are imposed, the average O/Ti ratio of the

Table 4:  $\text{Ti}_m\text{O}_x\text{C}_y\text{H}_z$  ( $m, x, y, z \in \mathbb{N}, m \geq 4$ ) species formed at the end of 6000 ps simulation of TTIP<sub>130</sub> reacting with 2340 O<sub>2</sub> molecules under different temperature profiles. The averaged C/Ti ratio and O/Ti ratio of the  $\text{Ti}_m\text{O}_x\text{C}_y\text{H}_z$  are listed.

$T$ profile	$\text{Ti}_m\text{O}_x\text{C}_y\text{H}_z$ ( $m \geq 4$ )	C/Ti	O/Ti
$T = 2500$ K (Case 4)	$\text{Ti}_6\text{O}_8\text{H}$ , $\text{Ti}_4\text{O}_7\text{H}$ , $\text{Ti}_4\text{O}_5\text{H}$ , $\text{Ti}_4\text{O}_5$ , $\text{Ti}_4\text{O}_4(5)^1$	0.00	1.18
$T_1$ (Case 7)	$\text{Ti}_{10}\text{O}_{22}\text{C}_2\text{H}_6$ , $\text{Ti}_{10}\text{O}_{17}\text{CH}_3$ , $\text{Ti}_8\text{O}_{14}\text{H}_7$ , $\text{Ti}_7\text{O}_{15}\text{CH}_4$ , $\text{Ti}_7\text{O}_{12}\text{H}_2$ , $\text{Ti}_6\text{O}_{15}\text{CH}_7$ , $\text{Ti}_4\text{O}_6\text{H}_3$ , $\text{Ti}_4\text{O}_5\text{H}_2$	0.09	1.89
$T_2$ (Case 8)	$\text{Ti}_9\text{O}_{19}\text{C}_3\text{H}_5$ , $\text{Ti}_7\text{O}_{12}\text{H}_3$ , $\text{Ti}_7\text{O}_{10}\text{H}_2$ , $\text{Ti}_6\text{O}_{12}\text{C}_2$ , $\text{Ti}_6\text{O}_{11}\text{H}_5$ , $\text{Ti}_6\text{O}_9\text{H}_3$ , $\text{Ti}_5\text{O}_{13}\text{C}_2\text{H}_2$ , $\text{Ti}_4\text{O}_{10}\text{CH}_5$ , $\text{Ti}_4\text{O}_9\text{CH}_2$ , $\text{Ti}_4\text{O}_4$	0.16	1.88
$T_3$ (Case 9)	$\text{Ti}_5\text{O}_7\text{C}$ , $\text{Ti}_4\text{O}_7\text{H}_3$ , $\text{Ti}_4\text{O}_6\text{H}_2$ , $\text{Ti}_4\text{O}_5\text{H}_2$	0.00	1.18
$T_4$ (Case 10)	$\text{Ti}_{20}\text{O}_{47}\text{C}_3\text{H}_{16}$ , $\text{Ti}_{11}\text{O}_{24}\text{CH}_6$ , $\text{Ti}_{11}\text{O}_{20}\text{CH}_5$ , $\text{Ti}_9\text{O}_{24}\text{C}_2\text{H}_5$ , $\text{Ti}_9\text{O}_{20}\text{CH}_{10}$ , $\text{Ti}_8\text{O}_{22}\text{C}_4\text{H}_5$ , $\text{Ti}_7\text{O}_{14}\text{CH}_7$ , $\text{Ti}_6\text{O}_{19}\text{C}_3\text{H}_4$ , $\text{Ti}_6\text{O}_{16}\text{CH}_8$ , $\text{Ti}_5\text{O}_{12}\text{H}_8$ , $\text{Ti}_5\text{O}_9\text{H}_3$ , $\text{Ti}_5\text{O}_8\text{H}$ , $\text{Ti}_4\text{O}_5\text{H}_2$	0.14	2.26
$T_5$ (Case 11)	$\text{Ti}_{15}\text{O}_{30}\text{C}_2\text{H}_{12}$ , $\text{Ti}_{11}\text{O}_{26}\text{CH}_8$ , $\text{Ti}_{11}\text{O}_{22}\text{CH}_5$ , $\text{Ti}_8\text{O}_{22}\text{C}_3\text{H}_5$ , $\text{Ti}_7\text{O}_{20}\text{C}_2\text{H}_7$ , $\text{Ti}_5\text{O}_{14}\text{CH}_3$ , $\text{Ti}_5\text{O}_{11}\text{H}_5$ , $\text{Ti}_4\text{O}_{11}\text{CH}_2$ , $\text{Ti}_4\text{O}_{10}\text{H}_6$ , $\text{Ti}_4\text{O}_7\text{H}_2$	0.06	1.47

<sup>1</sup> 5 in () represents there are 5  $\text{Ti}_4\text{O}_4$ . The quantity of all other species in the table is 1.

$\text{Ti}_m\text{O}_x\text{C}_y\text{H}_z$  ( $m \geq 4$ ) species obtained at the end of simulation can reach some value  $\approx 2$ . This observation is consistent with Figs. 12(b) and 12(c), which show that shorter high-temperature residence time can promote the formation of  $\text{Ti}_m\text{O}_x\text{C}_y\text{H}_z$  ( $m \geq 4$ ) species by promoting the condensation of  $\text{TiO}_2$  vapors. The average C/Ti ratio of  $\text{Ti}_m\text{O}_x\text{C}_y\text{H}_z$  ( $m \geq 4$ ) species provided in Table 4 can be used to measure the amount of carbon impurities in these incipient Ti-containing clusters under different temperature profiles. Generally, longer high-temperature residence time can reduce the hydrocarbon impurities in  $\text{Ti}_m\text{O}_x\text{C}_y\text{H}_z$  ( $m \geq 4$ ) species (see Case 4 and Case 9, where C/Ti = 0.0) as higher temperatures can effectively promote the break of C-O bonds. However, higher temperatures can also impede the formation of Ti-O bonds. This indicates the optimal temperature profile needs to be determined in order to obtain a relatively high production rate of  $\text{TiO}_2$  nanoparticle as well as relatively low carbon impurities.

#### 4. Conclusions

In this work, we studied the process of  $\text{TTIP}_{130}$  precursor droplet conversion to incipient Ti-containing clusters with or without gaseous  $\text{O}_2$  molecules at temperatures ranging from 1000 K to 2500 K using ReaxFF reactive molecular dynamics simulation. A new Ti/C/H/O ReaxFF force field was employed. Based on the simulation results, key intermediate titanium species are identified; The initial decomposition pathway of TTIP molecules and the growth pathway of incipient Ti-containing clusters are scrutinized. Eleven simulation cases with different conditions are designed to investigate the effect of temperature,  $\text{O}_2$  concentration and high-temperature residence time on the conversion of TTIP precursors to incipient titanium clusters. Main conclusions from this study can be summarized as follows:

- (1) Thermal decomposition of TTIP is mainly initiated by the break of Ti-O bond in TTIP, followed by C-O bond breaking at temperatures in the range of 1500 K to 2500 K. Comparing the time evolution of  $\text{TiO}_x\text{C}_y\text{H}_z$ ,  $\text{Ti}_2\text{O}_x\text{C}_y\text{H}_z$

and  $\text{Ti}_m\text{O}_x\text{C}_y\text{H}_z$  ( $x, y, z, m \in \mathbb{N}, m > 2$ ) species of TTIP<sub>130</sub> pyrolysis at 1500 K, 2000 K and 2500 K suggests that high temperature does not necessarily promote the formation of Ti-containing clusters, because the newly formed Ti-O bonds in  $\text{Ti}_2\text{O}_x\text{C}_y\text{H}_z$  species are less stable at high temperatures.

(2) For pyrolysis of TTIP<sub>130</sub> at temperatures ranging from 1500 K to 2500 K,  $\text{Ti}_2\text{O}_x\text{C}_y\text{H}_z$  ( $x, y, z \in \mathbb{N}$ ) species are found to appear earlier than  $\text{TiO}_2$  molecules and have much higher number concentration than  $\text{TiO}_2$ . In contrast, with 2340 gaseous  $\text{O}_2$  molecules being introduced, the number of  $\text{TiO}_2$  molecules increases significantly and  $\text{TiO}_2$  is formed earlier than  $\text{Ti}_2\text{O}_x\text{C}_y\text{H}_z$  species. By analyzing the time evolution of Ti-O bonds in the simulation system, it is suggested that  $\text{O}_2$  molecules can promote the breakup of original Ti-O bonds in TTIP molecules, and O atoms in  $\text{O}_2$  will replace the original O atoms in TTIP to form bond with Ti atoms. In addition, the amount of  $\text{TiO}_2$  is found to increase with increasing concentration of gaseous  $\text{O}_2$ .

(3) By comparing the results obtained with five different temperature profiles in the range of 1000 K – 2500 K being imposed during simulations of TTIP<sub>130</sub> reacting with 2340  $\text{O}_2$  molecules (i.e., equivalence ratio = 1), it is suggested that reducing high-temperature residence time facilitates the formation of incipient Ti-containing clusters by promoting the condensation process of  $\text{TiO}_2$  vapors, as the saturated vapor pressure of  $\text{TiO}_2$  declines with decreasing temperature.

(4) Ti, TiO, TiOH and  $\text{Ti}(\text{OH})_2$  are found to be major titanium intermediate species during pyrolysis of TTIP at temperatures higher than 2000 K, while TiO and  $\text{TiO}_2$  are identified as two dominant titanium species during TTIP<sub>130</sub> reacting with 2340 gaseous  $\text{O}_2$  molecules at 2500 K. However,  $\text{Ti}(\text{OH})_4$ , which was generally considered to be the major Ti-containing intermediate species in the TTIP conversion to  $\text{TiO}_2$ , is hardly observed based on our simulations, suggesting the conversion mechanism of TTIP to  $\text{TiO}_2$  vapors needs to be reconsidered at least for high-temperature regime.

(5) Incipient Ti-containing clusters grow up by forming Ti-O bond with  $\text{TiO}_x\text{C}_y\text{H}_z$  species or with another titanium cluster, i.e.,  $\text{Ti}_m\text{O}_x\text{C}_y\text{H}_z$  ( $x, y, z, m \in \mathbb{N}, m \geq 2$ ), followed by continuous breaking of Ti-O bonds or C-O bonds to re-

lease hydrocarbon moieties such as  $C_3H_7O$  and  $C_3H_6$ , etc. In addition,  $Ti_4O_4$  is identified to be a major building block of incipient Ti-containing clusters, as its number is significantly higher than other  $Ti_mO_xC_yH_z$  ( $m \geq 4$ ) species.

### Acknowledgement

This work was supported by the UK Engineering and Physical Sciences Research Council (EPSRC) under Grant Nos. EP/R029598/1 and EP/T015233/1, the National Natural Science Foundation of China (Grant No. 52106164), and the China Postdoctoral Science Foundation (Grant No. 2021M691728).

### References

- [1] H. Zhang, J. F. Banfield, Structural characteristics and mechanical and thermodynamic properties of nanocrystalline  $TiO_2$ , *Chemical Reviews* 114 (2014) 9613–9644.
- [2] Y. Wang, M. Zu, X. Zhou, H. Lin, F. Peng, S. Zhang, Designing efficient  $TiO_2$ -based photoelectrocatalysis systems for chemical engineering and sensing, *Chemical Engineering Journal* 381 (2020) 122605.
- [3] G. A. Kelesidis, S. E. Pratsinis, A perspective on gas-phase synthesis of nanomaterials: Process design, impact and outlook, *Chemical Engineering Journal* 421 (2021) 129884.
- [4] G.-J. Yang, C.-J. Li, S.-Q. Fan, Y.-Y. Wang, C.-X. Li, Influence of annealing on photocatalytic performance and adhesion of vacuum cold-sprayed nanostructured  $TiO_2$  coating, *Journal of thermal spray technology* 16 (2007) 873–880.
- [5] D. K. Fischer, K. R. de Fraga, C. W. Scheeren, Ionic liquid/ $TiO_2$  nanoparticles doped with non-expensive metals: new active catalyst for phenol photodegradation, *RSC Advances* 12 (2022) 2473–2484.

- [6] K. Sahner, M. Kaspar, R. Moos, Assessment of the novel aerosol deposition method for room temperature preparation of metal oxide gas sensor films, *Sensors and Actuators B: Chemical* 139 (2009) 394–399.
- [7] T. Suzuki, T. Ohgaki, Y. Adachi, I. Sakaguchi, Polarity reversal of resistance response to trace H<sub>2</sub> gas in the air between asymmetrically shaped electrodes on rutile-TiO<sub>2</sub> single crystal, *Journal of Applied Physics* 131 (2022) 034501.
- [8] J. O. Kim, W. Y. Choi, B. K. Choi, J. T. Jeong, Fabrication of photocatalytic TiO<sub>2</sub> thin film using innovative aerosol deposition method, in: *Materials science forum*, volume 510, Trans Tech Publ, 2006, pp. 1–4.
- [9] Y. Song, X. Lu, Z. Liu, W. Liu, L. Gai, X. Gao, H. Ma, Efficient removal of Cr(VI) by TiO<sub>2</sub> based micro-nano reactor via the synergy of adsorption and photocatalysis, *Nanomaterials* 12 (2022) 291.
- [10] H. Jami, A. Jabbarzadeh, Unravelling ultrafast deformation mechanisms in surface deposition of titanium nanoparticles, *Applied Surface Science* 489 (2019) 446–461.
- [11] H. Jami, A. Jabbarzadeh, Ultrafast thermomechanical effects in aerosol deposition of hydroxyapatite nanoparticles on a titanium substrate, *Surface and Coatings Technology* 382 (2020) 125173.
- [12] H. Jami, A. Jabbarzadeh, Molecular simulation of high-velocity deposition of titanium dioxide nanoparticles on titanium, *Applied Surface Science* 542 (2021) 148567.
- [13] L. Mädler, H. Kammler, R. Mueller, S. E. Pratsinis, Controlled synthesis of nanostructured particles by flame spray pyrolysis, *Journal of Aerosol Science* 33 (2002) 369–389.
- [14] S. E. Pratsinis, *History of manufacture of fine particles in high-temperature aerosol reactors*, RTI Press, 2011, pp. 475–507.

- [15] C. Schulz, T. Dreier, M. Fikri, H. Wiggers, Gas-phase synthesis of functional nanomaterials: challenges to kinetics, diagnostics, and process development, *Proceedings of the Combustion Institute* 37 (2019) 83–108.
- [16] S. E. Pratsinis, Flame aerosol synthesis of ceramic powders, *Progress in Energy and Combustion Science* 24 (1998) 197–219.
- [17] S. Li, Y. Ren, P. Biswas, D. T. Stephen, Flame aerosol synthesis of nanostructured materials and functional devices: Processing, modeling, and diagnostics, *Progress in Energy and Combustion Science* 55 (2016) 1–59.
- [18] F. Meierhofer, U. Fritsching, Synthesis of metal oxide nanoparticles in flame sprays: Review on process technology, modeling, and diagnostics, *Energy & Fuels* 35 (2021) 5495–5537.
- [19] W. Y. Teoh, R. Amal, L. Mädler, Flame spray pyrolysis: An enabling technology for nanoparticles design and fabrication, *Nanoscale* 2 (2010) 1324–1347.
- [20] K. B. Riad, P. M. Wood-Adams, K. Wegner, Flame-made TiO<sub>2</sub> (B), *Materials Research Bulletin* 106 (2018) 276–281.
- [21] J. Wei, Y. Ren, Y. Zhang, B. Shi, S. Li, Effects of temperature-time history on the flame synthesis of nanoparticles in a swirl-stabilized tubular burner with two feeding modes, *Journal of Aerosol Science* 133 (2019) 72–82.
- [22] A. Keller, I. Wlokas, M. Kohns, H. Hasse, Thermophysical properties of mixtures of titanium (iv) isopropoxide (TTIP) and p-xylene, *Journal of Chemical & Engineering Data* 65 (2020) 869–876.
- [23] P. Buerger, D. Nurkowski, J. Akroyd, S. Mosbach, M. Kraft, First-principles thermochemistry for the thermal decomposition of titanium tetraisopropoxide, *The Journal of Physical Chemistry A* 119 (2015) 8376–8387.

- [24] P. Buerger, D. Nurkowski, J. Akroyd, M. Kraft, A kinetic mechanism for the thermal decomposition of titanium tetraisopropoxide, *Proceedings of the Combustion Institute* 36 (2017) 1019–1027.
- [25] Y. Wang, P. Liu, J. Fang, W.-N. Wang, P. Biswas, Kinetics of sub-2 nm TiO<sub>2</sub> particle formation in an aerosol reactor during thermal decomposition of titanium tetraisopropoxide, *Journal of Nanoparticle Research* 17 (2015) 1–13.
- [26] Y. Ren, K. Ran, S. Kruse, J. Mayer, H. Pitsch, Flame synthesis of carbon metal-oxide nanocomposites in a counterflow burner, *Proceedings of the Combustion Institute* 38 (2021) 1269–1277.
- [27] C. Liu, S. Li, Y. Zong, Q. Yao, D. T. Stephen, Laser-based investigation of the transition from droplets to nanoparticles in flame-assisted spray synthesis of functional nanoparticles, *Proceedings of the Combustion Institute* 36 (2017) 1109–1117.
- [28] S. Memarzadeh, E. D. Tolmachoff, D. J. Phares, H. Wang, Properties of nanocrystalline TiO<sub>2</sub> synthesized in premixed flames stabilized on a rotating surface, *Proceedings of the Combustion Institute* 33 (2011) 1917–1924.
- [29] H. Chang, S. J. Kim, H. D. Jang, J. W. Choi, Synthetic routes for titania nanoparticles in the flame spray pyrolysis, *Colloids and Surfaces A: Physicochemical and Engineering Aspects* 313 (2008) 282–287.
- [30] H. Zhao, X. Liu, S. D. Tse, Effects of pressure and precursor loading in the flame synthesis of titania nanoparticles, *Journal of Aerosol Science* 40 (2009) 919–937.
- [31] H.-K. Ma, T.-J. Pan, P.-T. Cheng, et al., Numerical study of the nanoparticle formation mechanism in a titania flame combustion synthesis process, *Aerosol and Air Quality Research* 14 (2014) 251–259.

- [32] M. Y. Manuputty, J. Akroyd, S. Mosbach, M. Kraft, Modelling TiO<sub>2</sub> formation in a stagnation flame using method of moments with interpolative closure, *Combustion and Flame* 178 (2017) 135–147.
- [33] M. Y. Manuputty, C. S. Lindberg, J. A. Dreyer, J. Akroyd, J. Edwards, M. Kraft, Understanding the anatase-rutile stability in flame-made TiO<sub>2</sub>, *Combustion and Flame* 226 (2021) 347–361.
- [34] Z. Xu, H. Zhao, H. Zhao, CFD-population balance Monte Carlo simulation and numerical optimization for flame synthesis of TiO<sub>2</sub> nanoparticles, *Proceedings of the Combustion Institute* 36 (2017) 1099–1108.
- [35] C. Liu, J. Camacho, H. Wang, Phase equilibrium of TiO<sub>2</sub> nanocrystals in flame-assisted chemical vapor deposition, *ChemPhysChem* 19 (2018) 180–186.
- [36] B. Buesser, S. E. Pratsinis, Design of nanomaterial synthesis by aerosol processes, *Annual Review of Chemical and Biomolecular Engineering* 3 (2012) 103–127.
- [37] S. Tsantilis, H. Kammler, S. Pratsinis, Population balance modeling of flame synthesis of titania nanoparticles, *Chemical Engineering Science* 57 (2002) 2139–2156.
- [38] N. Baguer, E. Neyts, S. Van Gils, A. Bogaerts, Study of atmospheric MOCVD of TiO<sub>2</sub> thin films by means of computational fluid dynamics simulations, *Chemical Vapor Deposition* 14 (2008) 339–346.
- [39] K. Okuyama, R. Ushio, Y. Kousaka, R. C. Flagan, J. H. Seinfeld, Particle generation in a chemical vapor deposition process with seed particles, *AIChE Journal* 36 (1990) 409–419.
- [40] K. S. Ershov, S. A. Kochubei, V. G. Kiselev, A. V. Baklanov, Decomposition pathways of titanium isopropoxide Ti(OiPr)<sub>4</sub>: New insights from UV-photodissociation experiments and quantum chemical calculations, *The Journal of Physical Chemistry A* 122 (2018) 1064–1070.

- [41] A. Shmakov, O. Korobeinichev, D. Knyazkov, A. Paletsky, R. Maksutov, I. Gerasimov, T. Bolshova, V. Kiselev, N. Gritsan, Combustion chemistry of  $\text{Ti}(\text{OC}_3\text{H}_7)_4$  in premixed flat burner-stabilized  $\text{H}_2/\text{O}_2/\text{Ar}$  flame at 1 atm, *Proceedings of the Combustion Institute* 34 (2013) 1143–1149.
- [42] J. Fang, Y. Wang, J. Kangasluoma, M. Attoui, H. Junninen, M. Kulmala, T. Petäjä, P. Biswas, Cluster formation mechanisms of titanium dioxide during combustion synthesis: Observation with an APi-TOF, *Aerosol Science and Technology* 51 (2017) 1071–1081.
- [43] M. Y. Manuputty, J. A. Dreyer, Y. Sheng, E. J. Bringley, M. L. Botero, J. Akroyd, M. Kraft, Polymorphism of nanocrystalline  $\text{TiO}_2$  prepared in a stagnation flame: formation of the  $\text{TiO}_2$ -II phase, *Chemical Science* 10 (2019) 1342–1350.
- [44] A. Teleki, S. E. Pratsinis, Blue nano titania made in diffusion flames, *Physical Chemistry Chemical Physics* 11 (2009) 3742–3747.
- [45] A. C. Van Duin, S. Dasgupta, F. Lorant, W. A. Goddard, ReaxFF: a reactive force field for hydrocarbons, *The Journal of Physical Chemistry A* 105 (2001) 9396–9409.
- [46] Y. Zhang, S. Li, W. Yan, Q. Yao, S. D. Tse, Role of dipole–dipole interaction on enhancing brownian coagulation of charge-neutral nanoparticles in the free molecular regime, *The Journal of Chemical Physics* 134 (2011) 084501.
- [47] B. Buesser, A. Grohn, S. E. Pratsinis, Sintering rate and mechanism of  $\text{TiO}_2$  nanoparticles by molecular dynamics, *The Journal of Physical Chemistry C* 115 (2011) 11030–11035.
- [48] Y. Ren, Y. Zhang, Q. Mao, H. Pitsch, Amorphous-to-crystalline transition during sintering of nascent  $\text{TiO}_2$  nanoparticles in gas-phase synthesis: A molecular dynamics study, *The Journal of Physical Chemistry C* 124 (2020) 27763–27771.

- [49] Q. Mao, Y. Ren, K. H. Luo, S. Li, Sintering-induced phase transformation of nanoparticles: A molecular dynamics study, *The Journal of Physical Chemistry C* 119 (2015) 28631–28639.
- [50] T. P. Senftle, S. Hong, M. M. Islam, S. B. Kylasa, Y. Zheng, Y. K. Shin, C. Junkermeier, R. Engel-Herbert, M. J. Janik, H. M. Aktulga, et al., The ReaxFF reactive force-field: development, applications and future directions, *npj Computational Materials* 2 (2016) 1–14.
- [51] J. Wei, A. Ostadhossein, S. Li, M. Ihme, Kinetics for the hydrolysis of  $\text{Ti}(\text{OC}_3\text{H}_7)_4$ : A molecular dynamics simulation study, *Proceedings of the Combustion Institute* 38 (2021) 1433–1440.
- [52] S. Plimpton, Fast parallel algorithms for short-range molecular dynamics, *Journal of Computational Physics* 117 (1995) 1–19.
- [53] K. Chenoweth, A. C. Van Duin, W. A. Goddard, ReaxFF reactive force field for molecular dynamics simulations of hydrocarbon oxidation, *The Journal of Physical Chemistry A* 112 (2008) 1040–1053.
- [54] H. M. Aktulga, J. C. Fogarty, S. A. Pandit, A. Y. Grama, Parallel reactive molecular dynamics: Numerical methods and algorithmic techniques, *Parallel Computing* 38 (2012) 245–259.
- [55] W. Zhang, A. C. Van Duin, Improvement of the ReaxFF description for functionalized hydrocarbon/water weak interactions in the condensed phase, *The Journal of Physical Chemistry B* 122 (2018) 4083–4092.
- [56] K. Ganeshan, Y. K. Shin, N. C. Osti, Y. Sun, K. Prenger, M. Naguib, M. Tyagi, E. Mamontov, D.-E. Jiang, A. C. Van Duin, Structure and dynamics of aqueous electrolytes confined in 2D- $\text{TiO}_2/\text{Ti}_3\text{C}_2\text{T}_2$  MXene heterostructures, *ACS Applied Materials & Interfaces* 12 (2020) 58378–58389.
- [57] D. Zhang, M. Ashton, A. Ostadhossein, A. C. Van Duin, R. G. Hennig, S. B. Sinnott, Computational study of low interlayer friction in  $\text{Ti}_{n+1}\text{C}_n$

- ( $n = 1, 2,$  and  $3$ ) MXene, *ACS applied materials & interfaces* 9 (2017) 34467–34479.
- [58] A. Ostadhossein, J. Guo, F. Simeski, M. Ihme, Functionalization of 2D materials for enhancing OER/ORR catalytic activity in Li–oxygen batteries, *Communications Chemistry* 2 (2019) 1–11.
- [59] N. C. Osti, M. Naguib, K. Ganeshan, Y. K. Shin, A. Ostadhossein, A. C. Van Duin, Y. Cheng, L. L. Daemen, Y. Gogotsi, E. Mamontov, et al., Influence of metal ions intercalation on the vibrational dynamics of water confined between mxene layers, *Physical Review Materials* 1 (2017) 065406.
- [60] M. Mojtabavi, A. VahidMohammadi, K. Ganeshan, D. Hejazi, S. Shahbazmohamadi, S. Kar, A. C. Van Duin, M. Wanunu, Wafer-scale lateral self-assembly of mosaic  $\text{Ti}_3\text{C}_2\text{T}_x$  MXene monolayer films, *ACS Nano* 15 (2021) 625–636.
- [61] G. Plummer, B. Anasori, Y. Gogotsi, G. J. Tucker, Nanoindentation of monolayer  $\text{Ti}_{n+1}\text{C}_n\text{T}_x$  MXenes via atomistic simulations: The role of composition and defects on strength, *Computational Materials Science* 157 (2019) 168–174.
- [62] Wikipedia contributors, Titanium isopropoxide — Wikipedia, the free encyclopedia, 2021. URL: [https://en.wikipedia.org/w/index.php?title=Titanium\\_isopropoxide&oldid=1025129803](https://en.wikipedia.org/w/index.php?title=Titanium_isopropoxide&oldid=1025129803), [Online; accessed 28-October-2021].
- [63] L. Martínez, R. Andrade, E. G. Birgin, J. M. Martínez, Packmol: a package for building initial configurations for molecular dynamics simulations, *Journal of Computational Chemistry* 30 (2009) 2157–2164.
- [64] W. Humphrey, A. Dalke, K. Schulten, VMD: visual molecular dynamics, *Journal of Molecular Graphics* 14 (1996) 33–38.

- [65] A. Stukowski, Visualization and analysis of atomistic simulation data with ovito—the open visualization tool, *Modelling and Simulation in Materials Science and Engineering* 18 (2009) 015012.
- [66] M. Feng, H. Li, K. H. Luo, A molecular dynamics study on oxidation of aluminum hydride ( $\text{AlH}_3$ )/hydroxyl-terminated polybutadiene (HTPB) solid fuel, *Proceedings of the Combustion Institute* 38 (2021) 4469–4476.
- [67] M. Feng, H. Li, Q. Mao, K. H. Luo, P. Hellier, Fundamental study on mechanisms of thermal decomposition and oxidation of aluminum hydride, *The Journal of Physical Chemistry C* 123 (2019) 24436–24445.
- [68] Z. Bai, X. Z. Jiang, K. H. Luo, Effects of water on pyridine pyrolysis: A reactive force field molecular dynamics study, *Energy* 238 (2022) 121798.
- [69] B. Chen, Z.-J. Diao, H.-Y. Lu, Using the ReaxFF reactive force field for molecular dynamics simulations of the spontaneous combustion of lignite with the hatcher lignite model, *Fuel* 116 (2014) 7–13.
- [70] S. Agrawalla, A. C. Van Duin, Development and application of a ReaxFF reactive force field for hydrogen combustion, *The Journal of Physical Chemistry A* 115 (2011) 960–972.
- [71] A. Ostadhosseini, E. D. Cubuk, G. A. Tritsarlis, E. Kaxiras, S. Zhang, A. C. Van Duin, Stress effects on the initial lithiation of crystalline silicon nanowires: reactive molecular dynamics simulations using reaxff, *Physical Chemistry Chemical Physics* 17 (2015) 3832–3840.
- [72] C. S. Lindberg, M. Y. Manuputty, P. Buerger, J. Akroyd, M. Kraft, Numerical simulation and parametric sensitivity study of titanium dioxide particles synthesised in a stagnation flame, *Journal of Aerosol Science* 138 (2019) 105451.
- [73] C. S. Lindberg, M. Y. Manuputty, J. Akroyd, M. Kraft, A two-step simulation methodology for modelling stagnation flame synthesised aggregate nanoparticles, *Combustion and Flame* 202 (2019) 143–153.

- [74] C. S. Lindberg, M. Y. Manuputty, E. K. Yapp, J. Akroyd, R. Xu, M. Kraft, A detailed particle model for polydisperse aggregate particles, *Journal of Computational Physics* 397 (2019) 108799.